ETH

Eidgenössische Technische Hochschule Zürich
Swiss Federal Institute of Technology Zurich

MASTER THESIS

Few Electron Double Quantum Dots for a Circuit QED Architecture

Anna Stockklauser

Zurich, July 12, 2012

Quantum Device Lab
Nanophysics Group

Laboratory for Solid State Physics
ETH Zürich

Supervisors	Tobias Frey
	Dr. J. Basset
Professors	Prof. Dr. T. Ihn
	Prof. Dr. K. Ensslin
	Prof. Dr. A. Wallraff

Abstract

Recently, dipole coupling of a microwave resonator to a double quantum dot charge qubit was realized with coupling strengths on the order of $50\,\mathrm{MHz}$ [1]. In this experiment, high decoherence of the qubit is one of the main obstacles on the way to reach strong coupling. The quantum dots were operated in the many electron regime, which is suspected to be a source of decoherence. For this thesis, double quantum dot designs for operation in the few electron regime were introduced with the goal to improve decoherence. The lateral quantum dots were realized in a GaAs/AlGaAs heterostructure.

The tasks performed for this thesis were twofold. First, new sample wafers were characterized in terms of charge carrier density and mobility by van der Pauw measurements. In addition, the influence of a parallel conducting layer in the wafer structure was determined.

Second, new designs of few electron double quantum dots were characterized in transport measurements and optimized according to the results. The plunger gate shape and size were the most crucial design parameters to be adjusted and their influence on the sample properties was investigated in detail. The samples had to be optimized in terms of two main competing requirements: a high lever arm of the plunger gates and sufficient inter-dot tunneling coupling. It was found that while the lever arm of the plunger gates could easily be increased with the plunger gate area, this simultaneously reduced inter-dot tunneling coupling. This problem could be resolved by suitably adjusting the sample geometry, so that the improved designs provide both high plunger gate lever arms and sufficient tunneling coupling between the dots.

Acknowledgments

Contents

1   Circuit QED with Quantum Dots

Within the last decade, circuit quantum electrodynamics (QED) has emerged as a new research field [2]. Like the field of atomic cavity QED that has long been studied in atomic physics and quantum optics, it treats the interaction of light and matter [3]. In atomic cavity quantum electrodynamics a single atom is coupled to a single photon via an optical cavity [4]. In ciruit QED an artificial system such as a superconducting qubit serves as the atom, while the cavity is formed by a coplanar waveguide resonator. The interaction between the superconducting qubit and the microwave photon can be exploited for quantum information processing applications [5]. Significant accomplishments were realized with this system, e.g. strong coupling between qubit and resonator [6] or the implementation of different logical gates and protocols for quantum information processing [7, 8].

Recently, hybrid systems for quantum information processing have gained more and more attention because they might present a way to combine the advantages of different systems. Such an approach is the objective of this project: a semiconductor double quantum dot is coupled to a microwave resonator. In this circuit QED system, a quantum dot operated as a charge qubit functions as the artificial atom and resonator dot coupling is mediated by electric dipole interaction [9]. As a recent result of this project, dipole coupling of the quantum dot charge qubit to a microwave resonator has successfully been demonstrated experimentally by Frey et al. [10, 1]. They reported on a coupling strength of $g/2\pi \approx 50\,\mathrm{MHz}$.

While this result was very encouraging, the ultimate goal of the project is to reach strong coupling between qubit and resonator. This is fulfilled if the coupling strength is much larger than the decoherence and decay rates of both the qubit (γ) and the resonator (κ): $g \gg \gamma, \kappa$. The theory of coupling a resonator and charge qubit was derived in detail in by Childress et al. for quantum dots [9] and by Blais et al. for superconducting qubits [11]. The description for superconducting qubits is analogous to our system: the cooper pair box of the superconducting circuit is in our case replaced by the quantum dot charge qubit but the interaction Hamiltonian is of the same form. The conditions for strong coupling have not been fulfilled in the quantum dot-resonator system. In particular the high decoherence rate γ_2 of the qubit poses a major challenge [1].

This section gives an introductory overview of the employed system. First, the general architecture is introduced before each of the two coupled systems is described in more detail. The resonator is characterized in section 1.2 and suitable quantum dot designs for the charge qubit are discussed in section 1.3. In the work leading up to this thesis, we tried to work towards the strong coupling goal by introducing new quantum dot designs, which are hoped to improve decoherence as explained at the end of the section.

1.1   Implementation of the Circuit QED architecture

Quantum dots (QDs) are solid state structures in which charge carriers are confined in all three dimensions to a small region in space so that their energy levels are quantized and well separated [12]. Due to this quantization of energy, the dot exhibits various atomic properties and the double dot system can be compared to a di-atomic molecule. It is therefore a suitable system to function as the artificial atom in our circuit QED architecture. Many different types of quantum dots have been realized [12]. In this thesis, lateral quantum dots are discussed, which are formed in a two-dimensional electron gas (2DEG) embedded in a semiconductor heterostructure. The dots are defined within the 2DEG by negatively biased
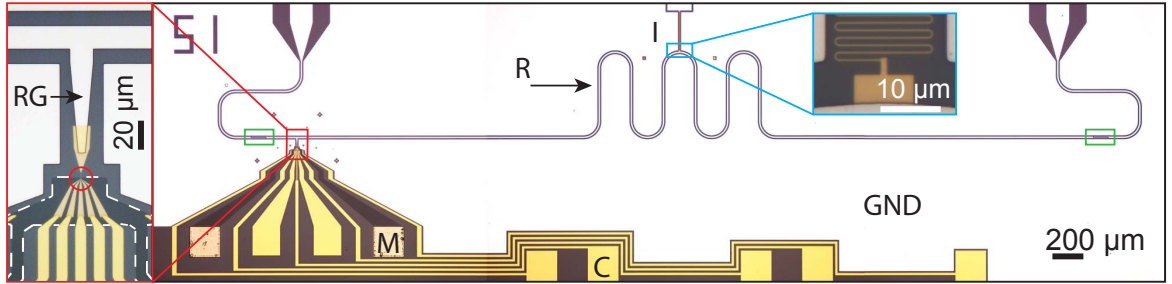
Figure 1: Optical microscope image of the on-chip resonator (R) with integrated quantum dot. The white area represents the aluminum ground plane (GND) of the resonator, its finger capacitors are located in the green boxes and the blue inset shows an inductor (I) as explained in the text. The inset framed in red shows the resonator gate (RG) extending to the quantum dot structure, which is positioned within the red circle. The contacts leading to the top gates are marked C and the ohmic contacts to the 2DEG are marked M.

top gate electrodes which the create electrostatic confinement and tunnel barriers of variable transmission.

The on chip resonator used in our experiment is a superconducting coplanar waveguide (CPW) resonator, in which a microwave field is confined between a center conductor and two ground planes [13]. To realize the circuit QED architecture, the double quantum dot structure and the coplanar waveguide resonator are integrated on one chip and coupled via a gate extending from the resonator to one of the dots.

The device geometry is shown in Fig. 1. The resonator (R) is coupled to input and output transmission lines via finger capacitors, which are indicated by the green rectangles in the figure. The resonator consists of a center conductor between two ground planes (GND), which cover most of the chip area. An inductor, which is magnified in the blue inset, connects the center conductor of the resonator to a voltage source. This ensures that the center conductor is not floating and enables biasing of the resonator. The quantum dot is positioned at an antinode of the electric field of the fundamental resonator mode as indicated by the red box in Fig. 1. The magnification shows the resonator gate (RG) that capacitively couples the CPW resonator to the double quantum dot sitting within the red circle. The top gates of the quantum dot structure are biased via the contacts labeled C and two ohmic contacts which are connected to the 2DEG are indicated by M. The employed double quantum dot structure is introduced at the end of the section. Details about the resonator design and its characteristic parameters are given in the following.

1.2 Resonator characterization

The ground plane and center conductor of the resonator are defined in a photo lithography process in which 3 nm Ti and 200 nm Al are deposited on the substrate. A schematic cross section of the resonator is shown in Fig. 2. In our samples, the gap (g) between the ground planes and the center conductor is designed to be 7.1 μm, the width (w) of the center conductor is 10 μm and the resonator length is 8205 μm excluding the finger capacitors. The substrate is formed by the GaAs/AlGaAs heterostructure, which holds the 2DEG for the lateral quantum
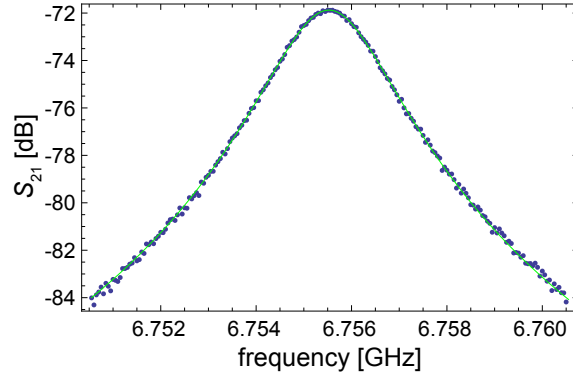
Figure 3: Transmission spectrum of the microwave resonator plotted vs. frequency. For the green curve, the measured transmission (S_{21}) was fitted using a Lorentzian fitting function.

dots. The 2DEG was, however, etched away for most of the chip area. The layer sequence of the substrate wafer is explained in detail in section 2.

A typical transmission spectrum of a microwave resonator is shown in Fig. 3, where the transmission S_{21} is plotted against the microwave frequency. The transmission exhibits a peak centered around a resonance frequency f_0. The fundamental resonance frequency is determined by the resonator length l and is given by [13]

Figure 2: Cross section of the resonator structure with a center conductor of width $w = 10\,\mu\text{m}$ and a gap $g = 7.1\,\mu\text{m}$ to the ground plane.

$$f_0 = \frac{c}{\sqrt{\epsilon_{\text{eff}}}}\frac{1}{2l}. \tag{1.1}$$

The wavelength of the fundamental mode is $\lambda_0 = 2l$, c denotes the vacuum speed of light and ϵ_{eff} is the effective permittivity of the transmission line.

The transmission spectrum has a Lorentzian line shape, which can be described by [13]

$$F_{\text{Lorentz}}(f) = A_0\frac{\delta f}{(f - f_0)^2 + \delta f^2/4}. \tag{1.2}$$

Here δf refers to the full width half maximum (FWHM) of the resonance and A_0 is a constant prefactor, which has to be determined by fits to measured data. The loaded quality factor of the resonator can also be extracted from the transmission spectrum as it is given by the ratio between f_0 and the FWHM [13]: $Q_{\text{L}} = f_0/\delta f$.

The transmission spectrum of the resonator was obtained by measuring the S-parameter $S_{21} = V_2^+/V_1^-$ as a function of microwave frequency using a vector network analyzer (VNA), where V_2^+ represents the voltage signal leaving the resonator at port 2 and V_1^- is the incoming signal at port 1. The S-parameter S_{21} is defined for the case in which no incoming signal is applied to port 2, so that it corresponds to the transmission of the system [14].

The coaxial cables of the VNA were only calibrated up to the instrument rack, not up to the cryostat. A power of -10 dBm was applied to port 1. The intermediate frequency (IF) bandwidth was set to 1 kHz. The total attenuation in our setup is approximately -90 dB. An

(a) Many electron design

(b) Few electron design

Figure 4: Two different double quantum dot designs for the operation as charge qubit. (a) Design used in previous experiments with top gates and a mesa edge to form the dots, a resonator gate and two additional plunger gates. (b) New few electron dot design, in which the dot is formed exclusively by top gates. The resonator gate functions as one of the plunger gates. A QPC is introduced as a charge detector.

amplifier at the 4.2 K temperature stage leads to an output signal gain of roughly 33 dB at a frequency of 7 GHz. Combined this yields an overall attenuation of -57 dB.

The measured transmission curve displayed in Fig. 3 exhibits the expected Lorentzian line shape centered around the resonance frequency $f_0 = 6.7555$ GHz. The data was fitted using Eq. (1.2), where data points down to -10 dB from the maximum were taken into account. The loaded quality factor resulting from the fit is $Q_\mathrm{L} = 2654.6 \pm 5.7$.

Only the fundamental resonance mode could be resolved. Resonances of the first (f_1) and second (f_2) mode are expected around 13.51 GHz and 20.26 GHz, respectively, but cannot be observed due to the setup bandwidth. The measurement was repeated for six different resonator gate voltages between 0 and -250 mV. However, no influence of the resonator bias on the transmission spectrum was observed. The resonance frequency did not shift and the FWHM remained unaffected.

1.3   Quantum dots as charge qubits

Fig. 4 shows two suitable double quantum dot designs for the circuit QED architecture. The design shown in Fig. 4(a) was used in the previous experiments [10, 1, 15], while design (b) was newly introduced for the experiments presented in this thesis. In the following, the principle of operating the double dots as charge qubits is explained. Furthermore, the differences between designs (a) and (b) and the considerations that lead to the introduction of a novel dot design are presented.

In both designs two dots are defined by top gates. In design (a) the electrons are in addition confined by a mesa edge represented by the white dashed line, above which the wafer structure is etched deep enough, that no 2DEG remains to hold the dot electrons. The regions connected to the ohmic contacts of source (S) and drain (D) are indicated in both figures as well as the resonator gates. The RG only overlaps with one of the two dots, which is necessary to enable dipole coupling to the resonator [9]. The different components of the QD structure are presented in detail in section 4.1.

(a)   (b)
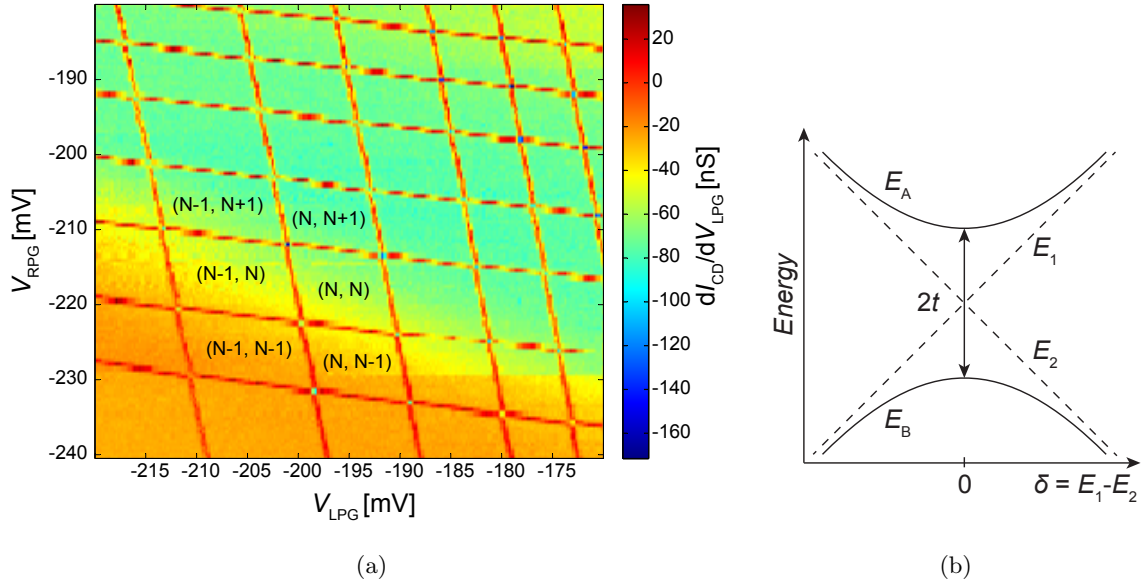
Figure 5: (a) Stability diagram of a double quantum dot. The areas within each hexagon correspond to the denoted charge configurations of the double dot system. The color scale denotes the transconductance measured with the right charge detector. (b) Energies of bonding (E_B) and antibonding (E_A) state of the two-level system formed by the double dot charge states. At zero detuning δ they have an energy difference of $2t$, where t describes the tunneling coupling of the two dots.

The charge state of the double dot system can be controlled by the left and right plunger gates, which are indicated by LPG ans RPG in the two figures. This principle is illustrated by the measurement of a so-called stability diagram presented in Fig. 5(a). The transconductance of the charge detector is shown in a 2D plot as a function of left and right plunger gate voltages. This kind of double dot measurements is discussed in detail in sections 3 and 4. Peaks in the transconductance form hexagons, where the points in the lower right and upper left corner of the hexagons are hardly separated in this measurement. By appropriately biasing the plunger gates, each dot can be charged or emptied, so that the area within each hexagon corresponds to a certain charge configuration of the two dots indicated in parentheses.

In a simplified model, the electron states in the double quantum dot can be described as a two-level system as it was for example derived in a review by van der Wiel et al. [16]. Only the energetically highest occupied levels of each dot are taken into account and the electrons are assumed not to interact with lower lying states. Furthermore, the influence of excited states in the two dots is neglected. We can therefore describe the separated dots by two eigenstates of energies E_1 and E_2. Tunneling coupling between the two dots leads to a delocalization of the two considered eigenstates of the individual dots so that a bonding and an antibonding state with energies E_A and E_B form [16]. These energies are plotted against the energy detuning $\delta = E_1 - E_2$ of the individual dots in Fig. 5(b). For zero detuning, the energy difference between the bonding and antibonding states is given by $2t$, where t is the tunneling coupling between the dots. For $t = 0$ we recover the energies of the unperturbed system E_1 and E_2, which are shown by the dashed lines.

The two-level system formed by the double quantum dot can therefore be considered in analogy to the two-level system formed by a superconducting cooper pair box. The theory

of a cooper pair box charge qubit coupled to a microwave resonator was e.g. described by Blais et al. [11] and can directly be transferred to the case of a quantum dot charge qubit. The energetic detuning δ of the two quantum dots is equivalent to the gate charge n_g in the cooper pair description. The tunneling coupling t between the dots has the function of the Josephson energy E_J in the cooper pair circuit QED model.

Using the particular dot design presented in Fig. 4(a) the quantum dot could only be operated as a charge qubit in the many electron regime with the number of electrons on each dot on the order of 100. As mentioned above, one of the main obstacles to reach strong coupling with the described architecture is high decoherence γ_2. One suspected reason for the low decoherence times are excited states in the many electron regime. While excited states are also present in quantum dots holding few electrons, they are much farther separated in energy in this case and therefore less likely to be populated, as derived in section 3. It is possible that closely spaced excited states in many electron quantum dots significantly diminish decoherence times.

For the work presented in this thesis, the dot designs were adapted to enable the operation of the QDs in the few electron regime with the goal of improving decoherence. The main difference between the few electron dot design shown in Fig. 4(b) and design (a) is that the dots can be formed using only top gates and no mesa edge. [This was desirable because it is suspected that the mesa edge makes it more difficult to empty the dots.] A second difference is the quantum point contact (QPC) that was placed next to the right dot. The QPC is employed as a charge detector in few electron transport measurements, which is explained in section 3.3.

The work on this thesis consisted of two main tasks. Different sample wafers were characterized using van der Pauw measurements and the new quantum dot designs were characterized in direct current (DC) transport measurements. Section 2 deals with the sample wafers, describing the theory behind the 2DEG and magnetotransport properties. The wafer structure and magnetotransport measurements are presented and the characteristic wafer properties are extracted. The next section provides an overview of the theory of transport measurements of single and double quantum dots. In section 4, the quantum dot measurements are presented. The first part deals with the employed samples describing the sample fabrication and the different characterized designs. Second, the results of the transport measurements are presented together with the extracted sample parameters for three different samples. Several problems that were encountered during these measurements are also discussed. Possible improvements were tested and are evaluated at the end of the section. The conclusions that could be drawn from these measurements are presented in the last section.

2   Wafer Characterization

Our samples were realized on semiconductor heterostructure wafers, which were grown by molecular beam epitaxy (MBE) [17, 18]. The performed transport experiments require a high mobility and sufficient carrier density [19]. The MBE growth of the semiconductor structures depends on many parameters, such as good vacuum and clean materials sources. The complexity of the process makes it difficult to predict the resulting wafer properties, which is why each wafer has to be characterized carefully.

In this section, the heterostructures are described in detail, starting with the formation of a 2DEG and magnetotransport in two dimensional systems. The results of van der Pauw measurements are presented, which were employed to extract interface charge densities and mobilities of the characterized wafer samples. Additionally, the dependence of the observed magnetotransport features on temperature and on top gate voltages are discussed.
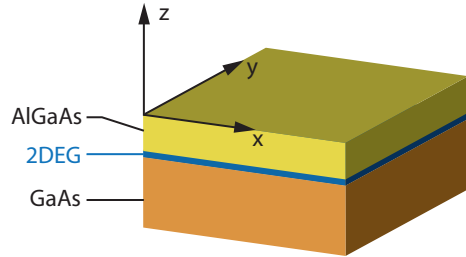
2.1   Two-dimensional electron gas

The two-dimensional electron gas builds the basis for the lateral quantum dot designs that were used in our experiments. In this section, the theoretical background of the 2DEG formation is explained following Nazarov and Blanter [20]. Typically, 2DEGs form at interfaces in selectively doped semiconductor heterostructures. An example of a suitable structure is a GaAs crystal covered by a layer of n-doped AlGaAs as depicted in Fig. 6.

Figure 6: Schematic AlGaAs/GaAS heterostructure with a 2DEG at the interface.

The intuitive explanation for the formation of a 2DEG at the interface between the two layers is that the electrons originating from the n-doping in AlGaAs travel to the weakly hole-doped GaAs side but remain close to the surface. The reason for this behavior lies in the band structure of GaAs and AlGaAs. The Fermi energies of the two materials have to align at the interface, which is made possible by band bending as shown in Fig. 7. The band gap of AlGaAs is larger than that of GaAs, so that a step in the conduction band edge occurs at the interface. The electrons from the AlGaAs side are trapped in the thus created triangular potential well. Due to this confinement in the z-direction they form a 2DEG in the x,y-plane.

In order to understand the conditions for the formation of a 2DEG in more detail, one needs to consider the electrostatic potential acting on the electrons. Because the structure is translationally invariant in x and y-direction the potential only depends on z. It can be calculated from the dopant densities in both materials and the resulting potential energy of the electrons in the conduction and valence band is shown in Fig. 7. For a sufficiently low dopant density in the AlGaAs, the potential in z-direction is parabolic on the AlGaAs side of the interface. The electrostatic potential jumps at the AlGaAs/GaAs interface due to the finite surface charge density of the 2DEG. On the GaAs side, band bending occurs within a depletion layer, which is free from holes, and the potential is constant in the rest of the crystal.

With the volume density of the dopants in AlGaAs given by n_1 and that of the dopants in GaAs by n_2, Nazarov and Blanter [20] calculate the sheet density of the electrons in the
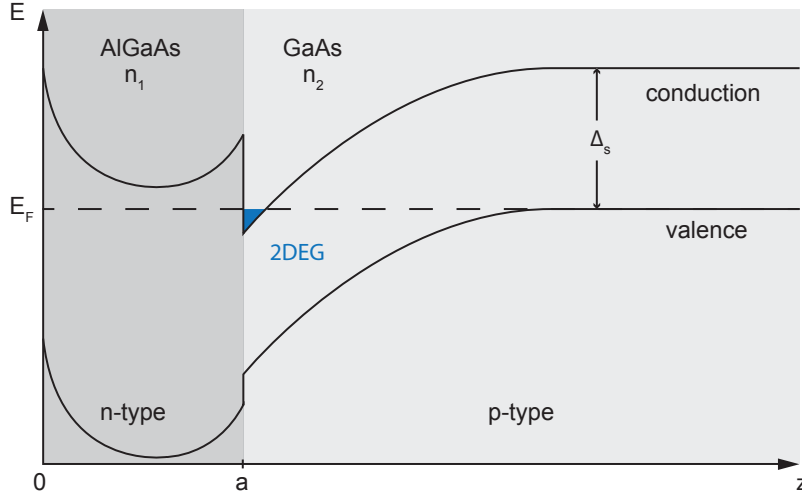
Figure 7: Conduction and valence band edges in a heterostructure of n-doped AlGaAs and p-doped GaAs depending on the z-position. A 2DEG forms in the triangular potential well bordering the interface.

2DEG to be

$$n_{\rm s} = n_1 a - \sqrt{\frac{\Delta_{\rm s} n_2 \epsilon \epsilon_0}{2\pi e^2}}. \tag{2.1}$$

Here, $\Delta_{\rm s}$ is the energy gap of GaAs and a the thickness of the AlGaAs layer, as indicated in Fig. 7, while $\epsilon_0 = 8.854 \times 10^{-12}$ F/m denotes the vacuum permittivity, which is multiplied by the relative permitivity of GaAs, $\epsilon = 12.9 \pm 0.2$. This equation essentially expresses charge conservation as the dopant concentrations on both sides determine the sheet density of the charges at the interface. Because the electrostatic potential acting on the electrons only depends on the z-direction, the electron motion in the x, y-plane is free. We can therefore describe the system as a two dimensional gas of free electrons.

The main difference between our wafer and the simple structure presented in Fig. 6 concerns the n-doped layer. The layer sequence of our wafer is depicted in Fig. 8. The $Al_x Ga_{1-x} As$ layer is not volume doped, but encloses a δ-donor layer, which is separated from the interface with the GaAs side by a 40 nm spacer layer of undoped $Al_x Ga_{1-x} As$. This spacer layer is advantageous as it reduces electron-dopant scattering [19] and leads to a higher mobility of the charge carriers in the 2DEG. The resulting band structure is very similar, however, so that a 2DEG develops at the $Al_x Ga_{1-x} As$/GaAs interface, in analogy to Fig. 7. The spacer layer is bordered by a Si δ-doped layer and another 45 nm of $Al_x Ga_{1-x} As$. The structure is topped by a cap layer of 5 nm GaAs. Together, this yields a depth of the 2DEG of 90 nm.

2.2 Magnetotransport properties

Within the theory of diffusive classical transport, conductance properties of two-dimensional electron systems are well described by the Drude model [19]. For transport in an external magnetic field B applied perpendicular to the 2DEG, the Drude model predicts the longitudinal component of the resistivity tensor to be $\rho_{xx} = 1/n_{\rm s}|e|\mu$. Therefore, ρ_{xx} is inversely proportional to both the electron density $n_{\rm s}$ and the mobility μ, but independent of magnetic field. The transverse or Hall resistivity is given by $\rho_{xy} = B/|e|n_{\rm s}$, which is linear in magnetic
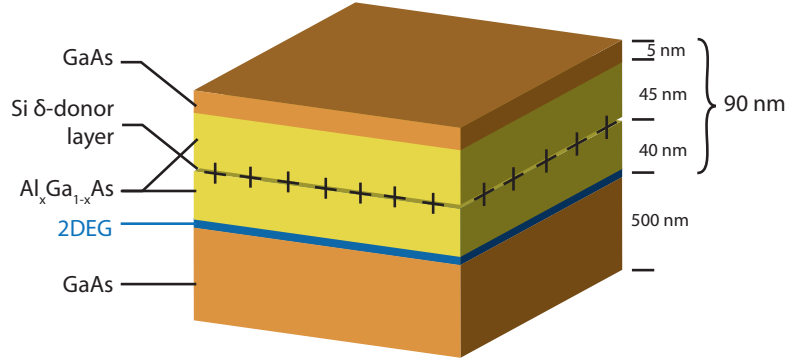
Figure 8: Layer sequence of our δ-doped heterostructure with a 2DEG 90 nm below the surface.

field. The Drude model proves accurate only for small fields, because it neglects the quantization of electron states in external magnetic fields [19]. Due to the quantization, first the longitudinal and for higher fields both resistivities oscillate around the classically predicted values. In this section, a derivation of these effects is outlined following Ihn [19].

The motion of electrons confined to the x, y-plane in an external magnetic field $\mathbf{B}=(0,0,B)$ in z-direction can be described by cyclotron orbits with quantized radii around a center coordinate $y_0 = \hbar k_x/eB$, where k_x is the wavevector in x-direction of the sample. This can be derived by solving the Schrödinger equation of an electron in a potential $V(z)$ in growth direction of the wafer. The equation has the form of a quantum mechanical harmonic oscillator and yields the energy eigenvalues

$$E_n = \hbar\omega_\mathrm{c}(n + 1/2) \tag{2.2}$$

for integer numbers n, where $\omega_\mathrm{c} = |e|B/m^*$ is the cyclotron frequency. These eigenstates are degenerate in the quantum number k_x and form the so-called Landau levels. The degeneracy of each level n is limited by the sample dimensions, as the center coordinate needs to lie within the sample. With this condition, the number of occupied Landau levels is found to be $\nu = hn_\mathrm{s}/|e|B$, which is called the filling factor. When the Zeeman splitting is negligible compared to $\hbar\omega_\mathrm{c}$, each Landau level can host two electrons per allowed k_x value.

Due to the discrete Landau levels, both the Fermi energy of the 2DEG and its scattering broadened density of states (DOS) oscillate periodically in $1/B$ for fixed electron densities. This oscillation of the DOS induces a modulation of the longitudinal resistivity ρ_{xx} around the classical value, which are known as Shubnikov-de Haas (SdH) oscillations. Therefore, the Shubnikov-de Haas oscillations are also periodic in $1/B$ and minima occur at even filling factors due to the spin degeneracy.

At higher magnetic fields ρ_{xx} vanishes at the minima and the Hall resistivity ρ_{xy} develops pronounced plateaus centered at even filling factors. This is attributed to the quantum Hall effect [21]. Therefore, $\rho_{xx}^{\mathrm{plateau}} = 0$, while the plateaus are found at fractions of the resistance quantum $h/e^2 \approx 25.813\,\mathrm{k\Omega}$:

$$\rho_{xy}^{\mathrm{plateau}} = \frac{h}{ie^2}, \tag{2.3}$$

where i is an integer. Again, the plateaus, respectively minima, are centered around magnetic
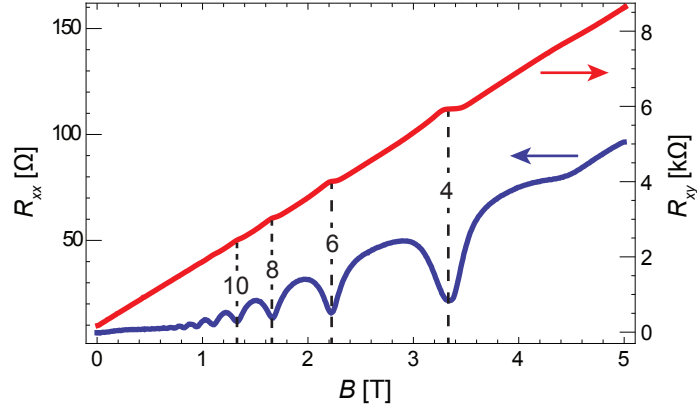
Figure 9: Measured longitudinal (in blue) and Hall resistance (in red) depending on the magnetic field showing Shubnikov-de Haas oscillations for $B < 1\,\text{T}$ and plateaus from the quantum Hall effect for higher fields. The filling factors are indicated (data from wafer ES 2062 measured at $4.2\,\text{K}$).

field values corresponding to even integer filling factors $\nu = i$:

$$B_i = \frac{n_\text{s} h}{i|e|}. \tag{2.4}$$

Oscillations of R_{xx} and R_{xy} in both the Shubnikov-de Haas ($B < 1\,\text{T}$) and the quantum Hall regime ($B > 1\,\text{T}$) are shown in Fig. 9 with the filling factors indicated. The minima of R_{xx} do not vanish in the quantum Hall regime above $1\,\text{T}$. Reasons for this behavior are discussed in the following sections. The $0\,\text{T}$ value of R_{xx} and slope of R_{xy} correspond to the classically predicted values around which they oscillate in a 1/B periodic fashion.

2.3   Van der Pauw measurements

Measurements of the longitudinal and transverse resistivity with the so-called van der Pauw method permit to experimentally determine the density and mobility of the charge carriers in the 2DEG. The method is based on four-point measurements and has the advantage that it can be employed for arbitrary sample geometries [19]. In our case, the wafer geometry was roughly a square with four Ohmic contacts placed close to the sample edges in the corners. It is schematically shown in Fig. 10.

Figure 10: Sample geometry with ohmic contacts A, B, C, D for the four-point measurement.

To determine the Hall resistivity, a current is injected at one contact and extracted from the one lying diagonally across from it, e.g. A and C, while the voltage drop is measured between the remaining two contacts, e.g. B and D. We find the Hall resistivity by averaging over the resistance values obtained for the two different combinations [19]:

$$\rho_{xy}(B) = \frac{1}{2}[R_{\text{AC,BD}}(B) - R_{\text{AC,BD}}(0) + R_{\text{BD,AC}}(B) - R_{\text{BD,AC}}(0)]. \tag{2.5}$$

Table 1: Charge densities and mobilities extracted from van der Pauw measurements. Two types of wafers with a different depth d of the 2DEG and a different doping method were characterized.

Wafer	d [nm]	Si δ-doping [cm^{-2}]	n_s [10^{11} cm^{-2}]	μ [$\frac{\mathrm{cm}^2}{\mathrm{Vs}}$]
EV 1681	90	5×10^{12}	0.52	3.78×10^4
EV 1720	100	vol. doped	0.75	5.70×10^4
EV 1723	90	1×10^{13}	0.59	4.48×10^4
EV 1728	90	2×10^{13}	1.04	6.60×10^4
EV 1732	100	vol. doped	0.52	4.50×10^4
EV 1734	100	vol. doped	0.25	0.42×10^4
EV 1738	100	vol. doped	0.63	4.42×10^4
ES 2062	90	5×10^{12}	3.47	4.89×10^5
ES 2074	90	5×10^{12}	3.47	5.42×10^5

The longitudinal component of the resistivity tensor, ρ_{xx}, can be measured using a current between two contacts on one edge of the sample and measuring the voltage drop at the opposite edge. The obtained resistances, $R_{\mathrm{AB,CD}}$ and $R_{\mathrm{AD,BC}}$ then yield [19]

$$\rho_{xx} = \frac{\pi}{\ln 2} \frac{R_{\mathrm{AB,CD}} + R_{\mathrm{AD,BC}}}{2} f\left(\frac{R_{\mathrm{AB,CD}}}{R_{\mathrm{AD,BC}}}\right). \tag{2.6}$$

In this expression the sample geometry is taken into account through a geometry factor f, which should be unity for square samples and is reduced for rectangles. Using the expressions predicted for the resistivities by the Drude model as discussed in the previous section, the charge density and mobility can be extracted as

$$n_\mathrm{s} = \frac{1}{|e|} \left(\frac{\mathrm{d}\rho_{xx}}{\mathrm{d}B}\bigg|_{B=0}\right)^{-1} \quad \text{and} \quad \mu = \frac{1}{n_\mathrm{s}|e|\rho_{xx}(B=0)}. \tag{2.7}$$

We employed the van der Pauw method to characterize new wafers. We first tested a series of wafers from a defective MBE machine, which are named EV in the following. The ES wafers originated from a different, functioning MBE machine. The measurements were performed at $4.2\,\mathrm{K}$ with magnetic fields up to $5\,\mathrm{T}$.

The mobilities and carrier densities that were extracted from the measurements are summarized in table 1. Only the samples EV 1681, EV 1723 and EV 1728 and both ES samples were grown according to the usual growth protocol of the δ-doped heterostructure shown in Fig. 8. The other samples were volume doped but can be used for comparison as we would expect similar results for density and mobility. All EV samples exhibit densities and mobilities clearly below what is expected from the intended doping and what is minimally required for our purposes, which is roughly $n_\mathrm{s} \approx 3 \times 10^{11}\,\mathrm{cm}^{-2}$ and $\mu \approx 5 \times 10^5\,\mathrm{cm}^2/\mathrm{Vs}$.

Wafer EV 1681 was grown according to the original protocol and the Si dopant concentration was twice increased by a factor of 2 for wafers EV 1723 and EV 1728. While a slight improvement in both density and mobility was observed, it was not sufficient. The volume doped test wafers did also not yield more positive results.

The ES wafers were again grown according to the original growth protocol. However, for these samples density and mobility are both increased by roughly a factor of ten with respect to wafer EV1681. This difference in wafer quality is also displayed in the measurements of

(a) Wafer EV 1728   (b) Wafer ES 2062
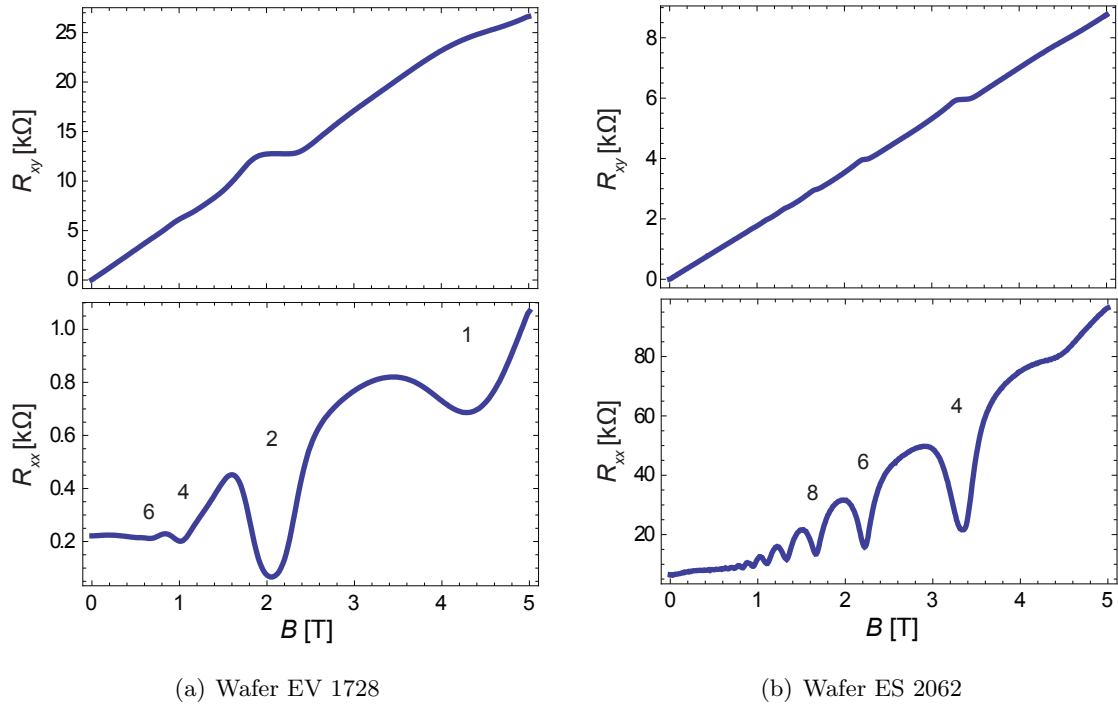
Figure 11: Plots of R_{xx} (bottom) and R_{xy} (top) versus magnetic field at $4.2\,\mathrm{K}$ for two wafers. The filling factors are denoted.

R_{xx} and R_{xy} in dependence of B, which are shown in Fig. 11 for the best EV and ES wafers. For the ES wafer, oscillations in R_{xx} are much more pronounced and visible up to high filling factors or down to small magnetic fields, respectively. For the EV wafer only oscillations up to a filling factor of 6 are discernible. Correspondingly, more plateaus are discernible in R_{xy}.

Most wafers were measured at $4.2\,\mathrm{K}$. To demonstrate the influence of temperature, wafer EV 1738 was additionally measured at $1.2\,\mathrm{K}$. The recorded Hall voltage and ρ_{xx} for magnetic fields between -5 and $5\,\mathrm{T}$ are shown in Fig. 12. The extracted conduction properties are independent of temperature, but all features are much more pronounced for the low temperature measurement. The $1.2\,\mathrm{K}$ curve exhibits quantum Hall plateaus starting below $1\,\mathrm{T}$, while hardly any plateaus can be observed in the $4.2\,\mathrm{K}$ curve. The oscillations in R_{xx} are much stronger so that one minimum vanishes, which is a signature of the quantum Hall effect that could not be observed at $4.2\,\mathrm{K}$.

2.4 Gate voltage dependence of conduction properties

The ES wafers had good densities and mobilities but the measurements of R_{xx} show a rising background in addition to the oscillations (see Fig. 11(b)). The minima of the oscillations are expected to reach zero in the regime of the quantum Hall effect, which is not given here. This can partially be attributed to the relatively high measurement temperature of $4.2\,\mathrm{K}$. Another origin of the rising background could be a parallel conducting layer, which can occur in heterostructures in addition to the 2DEG. Typically, a second occupied subband develops in the $Al_xGa_{1-x}As$ layer due to high dopant concentrations.

It is found that the second subband gives rise to an addtional term in the classically
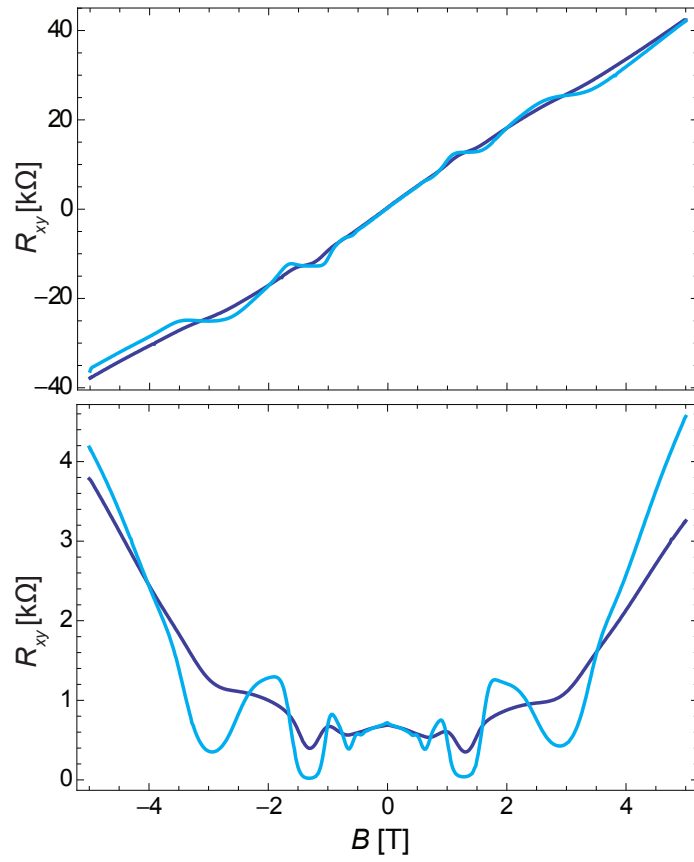
Figure 12: Measured longitudinal (bottom) and Hall resistance (top) depending on the magnetic field at $4.2\,\mathrm{K}$ (dark blue) and $1.2\,\mathrm{K}$ (cyan). (data from wafer EV 1738).
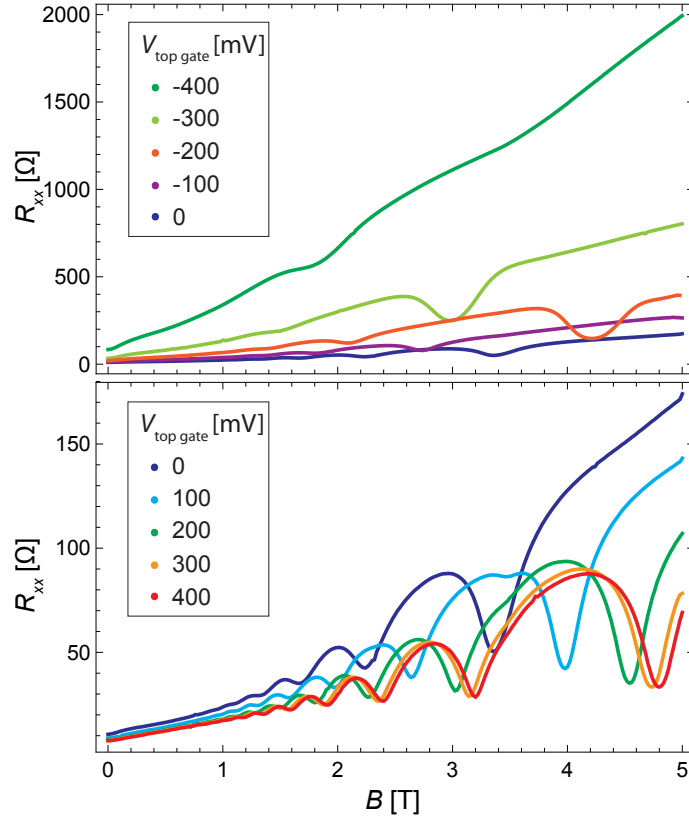
Figure 13: Plots of R_{xx} for positive and negative gate voltages (data from wafer ES 2074).

expected longitudinal resistivity [22, 23]:

$$\rho_{xx}^{\text{classical}}(B) = \rho_{xx}(0)\{1 + \frac{\mu n_{\text{s}}\mu_{\text{p}} n_{\text{p}}(\mu - \mu_{\text{p}})^2 B^2}{(\mu n_{\text{s}} + \mu_{\text{p}} n_{\text{p}})^2 + [\mu_1 \mu_{\text{p}}(n_{\text{s}} - n_{\text{p}})B]^2}\}, \tag{2.8}$$

where μ_{p} and n_{p} are the mobility and sheet density of the electrons in the parallel conducting layer. Because the densities and mobilities are fixed parameters of our system, the additional background is proportional to $B^2$ for small magnetic fields and approaches a constant value for large B. The value of $\rho_{xx}(0)$ is expected to equal the classical Drude result $1/n_{\text{s}}e\mu$. The SdH and quantum Hall oscillations, which have quantum mechanical origin, are added to this classical background.

Using a biased top gate the second subband can be depleted earlier than the 2DEG, which lies lower in the wafer. Measurements of the magnetoresistance for different top gate voltages are therefore a suitable method to test for a parallel conducting layer. To investigate the influence of top gate voltages on the wafer properties, we performed van der Pauw measurements for several positive and negative gate voltages. Some of the resulting curves for ρ_{xy} are shown in Fig. 13. The position of the minima corresponding to a fixed filling factor shifts to the left as more negative gate voltages are applied, which can be observed in both plots. This indicates a decrease of the electron density with more negative gate voltages as it is expected.

Gate voltage dependent measurements of the Hall resistance were also performed and used to extract the carrier density. The resulting densities n_{s} and mobilities μ are plotted versus

(a) Charge carrier density

(b) Mobility

(c) Leakage current to the 2DEG
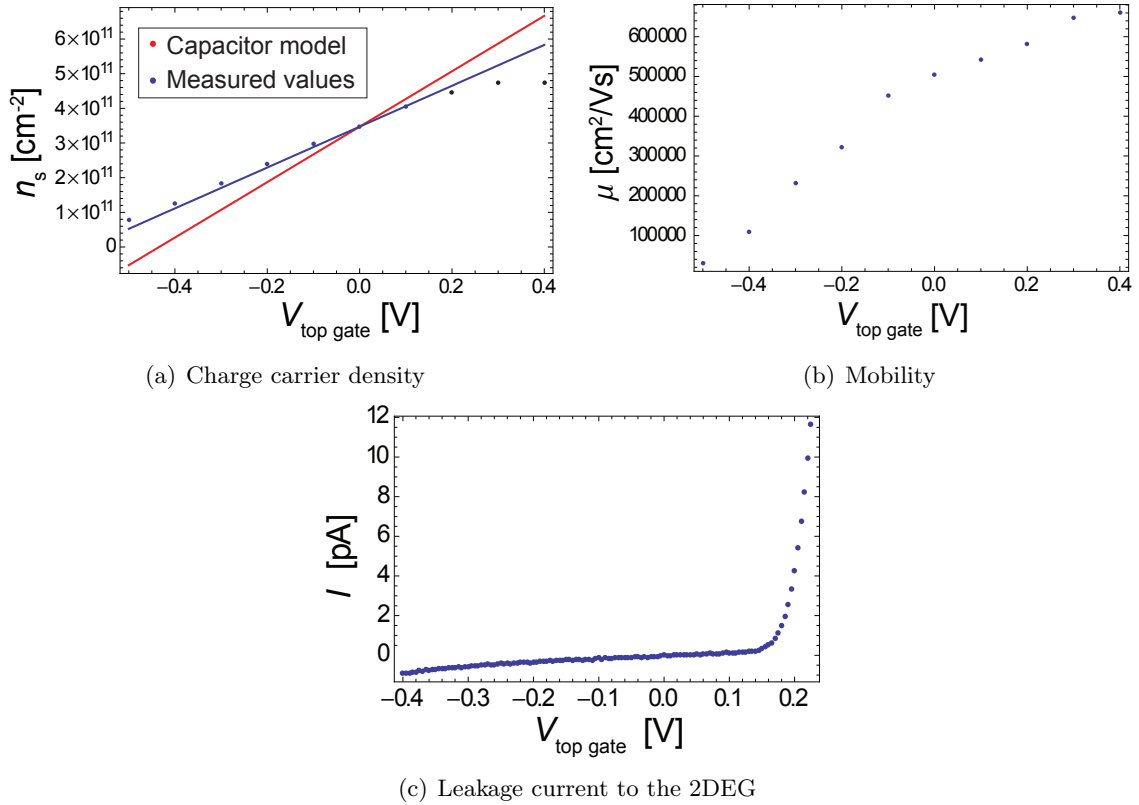
Figure 14: Plots of (a) the charge carrier density n_s of the 2DEG, (b) the mobility μ and (c) the leakage current between top gate and 2DEG as a function of top gate voltage.

top gate voltage in Fig. 14(a) and (b). Both density and mobility rise with increasing gate voltage in a roughly linear fashion but level off for positive gate voltages. At $V_{\text{top gate}} = 0$ the density measured for this sample with top gate was $n_s = 3.47 \times 10^{11}\,\text{cm}^{-2}$, while the mobility was $\mu = 5.42 \times 10^5\,\text{cm}^2/\text{Vs}$.

In a simplified picture, the increase of density with more positive bias can be explained by a capacitor model in which the 2DEG and the gate are regarded as the two plates of a parallel plate capacitor. The capacitance can be expressed in terms of the surface density of the electrons:

$$C = \frac{Q}{V} = \frac{n_s^{\text{cap}}|e|A}{V} = \frac{\epsilon\epsilon_0 A}{d}, \tag{2.9}$$

where A is the area covered by the top gate and d is the depth of the 2DEG.

Equation (2.9) can be rewritten as

$$n_s^{\text{cap}} = \frac{\epsilon\epsilon_0}{d|e|}V. \tag{2.10}$$

Inserting d=90 nm and ϵ=12.9 for GaAs, one finds a linear dependence of the density on the bias. Choosing the measured electron density at zero gate voltage as a reference value yields $n_s(V) = n_s^{\text{cap}}(V) + n_s^{\text{meas}}(0)$.

This curve is plotted in red in Fig. 14(a) along with a linear fit to the measured density values, which is shown in blue. The last three data points corresponding to voltages above

150 mV were excluded from the fitted data. The deviation of these points from the linear fit is due to a leakage current from the gate to the 2DEG, which sets in above +150 mV. This was concluded from a measurement of the leakage current, which presented in Fig. 14(c).

The relative deviation of the slopes of the fit and the capacitor model, which can be used as a measure for the occupancy of the second subband, is 26% for the presented data. This deviation is in part expected because Eq. (2.9) represents a simplified model. In reality, the effective separation between 2DEG and top gate is larger than the physical distance. The center of mass of the wave function of the 2DEG electrons does not sit at the interface but is shifted to the GaAs side by roughly 7 nm in our system. This is derived in Ref. [19]. A contribution of the so-called quantum capacitance adds another 2.5 nm to the effective separation [19]. Considering that the physical distance in our system is 90 nm, the additional 9.5 nm account for roughly 10% of the deviation. The comparison with the capacitor model, therefore, yields a reasonably good result and the parallel conducting channel cannot be identified as a serious problem in this wafer.

If the second subband was the main reason for the rising background, one would expect the background to vanish for more negative voltages as the parallel conducting layer is depleted. This is not observed in Fig. 13, which agrees with above conclusion. Instead, the background probably has to be attributed to the contribution of ρ_{xy} to the measured resistivity, which arises due to the fact that we do not have a perfect Hall bar geometry [19]. This explains why the slope of the background increases with more negative bias as the slope of ρ_{xy} increases with decreasing electron density.
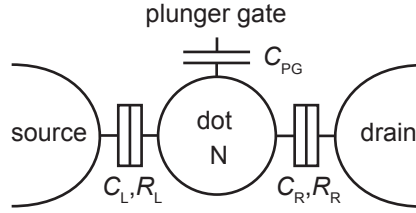
Figure 15: Illustration of a model of a single quantum dot, which is separated from source and drain by tunable tunnel barriers and capacitively coupled to a plunger gate.

3   Transport through Quantum Dots

For this thesis, different designs of single and double quantum dots were characterized in transport measurements. The theory necessary to understand the measurements is presented here. First, the relevant energy scales in a single dot structure are explained and the Coulomb blockade effect is introduced. Second, double quantum dot measurements of stability diagrams are discussed and the characteristic electrostatic parameters in a double dot system are derived from a capacitor model. The last section deals with quantum point contacts employed as charge detectors.

3.1   Single quantum dots

A schematic illustration of a single quantum dot is shown in Fig. 15. Adjustable tunnel barriers define the QD by confining electrons to a small two-dimensional region. The tunnel barriers couple the dot capacitively and resistively to source and drain with C_L, R_L and C_R, R_R, respectively (see Fig. 15). A bias applied between source and drain can induce transport through the dot. A plunger gate (PG) that is capacitively coupled to the dot by C_PG is used to tune the energy of the electrons in the dot. For a constant bias, electron transport can be controlled by the tunnel barriers and the plunger gate voltage.

In this section, the relevant energy scales arising in the quantum dot are discussed. In addition, the Coulomb blockaded transport regime is explained. The discussion in this section largely follows Ihn [19] and Kouwenhoven et al. [12].

3.1.1   Relevant energy scales

Mainly four different energy scales are relevant in quantum dot systems, which are related to the Coulomb energy, the coupling of the dot to the leads, the confinement energy and temperature. Because energy considerations are necessary to understand the characteristics of QD transport, this part provides an overview of the origin and order of magnitude of these energies as presented in Ref. [19].

Let us first motivate the origin of the so-called charging energy. The addition of an electron to the quantum dot requires sufficient energy to overcome the Coulomb repulsion due to the presence of the other electrons in the dot. The electrostatic energy arising from the Coulomb repulsion between N electrons in a 2DEG quantum dot system can be estimated as

$$E_\mathrm{elstat}(N) = \frac{e^2 N^2}{2C} \propto \frac{N^2}{r}. \tag{3.1}$$

The self-capacitance C of the quantum dot, which is approximated as a metallic disc, is given by $C = 8\epsilon\epsilon_0 r$, where r is the dot radius and ϵ is the relative dielectric constant of the material that holds the dot. The energy needed to add an $(N+1)$th electron to a dot with N electrons is, therefore, given by

$$\Delta E_{\text{elstat}}(N + 1) = E_{\text{elstat}}(N + 1) - E_{\text{elstat}}(N) \approx \frac{e^2 N}{C} \propto \frac{N}{r}, \tag{3.2}$$

where the approximation holds for large electron numbers N. The **charging energy** is defined as the difference

$$E_{\text{C}} = \Delta E_{\text{elstat}}(N + 1) - \Delta E_{\text{elstat}}(N) = \frac{e^2}{C}. \tag{3.3}$$

It is independent of the number of electrons on the dot as long as the condition of large N is fulfilled, i.e. in the many electron regime.

The charging energy in our system can be estimated by approximating the self-capacitance of the dot. Considering the dimensions of the top gates defining our lateral quantum dot presented in Fig. 4(b), it seems reasonable to approximate the dot radius as 100 nm. Furthermore, the relative dielectric constant of GaAs is roughly $\epsilon = 13$, which together yields a charging energy of 1.7 meV.

The charging energy given in Eq. (3.3) can only be measured if the number of charges on the dot is quantized. The condition for this is that the dot is only weakly tunnel coupled to the leads, i.e. that the tunneling resistances R_{L} and R_{R} are considerably higher than the resistance quantum: $R_{\text{L/R}} > h/e^2$. Thus, QD transport experiments require low tunneling coupling to source and drain.

Another relevant energy scale is defined by the quantization of the electron energies due to their spacial confinement in the dot. With m^* the effective mass of the electrons in the dot, the **confinement** or **quantization energy** can be estimated as

$$E_{\text{conf}}(N) = \frac{\hbar^2}{2m^*} \frac{N^2}{r^2}. \tag{3.4}$$

This expression only holds for systems with parabolic dispersion relation, which is fulfilled for our two-dimensional electron gas. The confinement energy gives rise to discrete energy levels of the dot electrons. The spacing between successive single-particle levels is

$$\Delta = \frac{\hbar^2}{m^*} \frac{1}{r^2}. \tag{3.5}$$

Again using r=100 nm provides an estimate of the single-particle level spacing in GaAs dots: $\Delta \approx 110\,\mu\text{eV}$. This is about an order of magnitude smaller than the charging energy found above.

The quantized energy levels of each electron appear as excited states in our QD systems. As the level spacing inversely depends on r^2, small QDs exhibit a higher single-particle level spacing than large dots. Few electron dots are usually confined to a smaller region than dots operated in the many electron regime. For this reason, the energy levels of the excited states are much farther separated in few electron QDs as shown in section 4.2.

Generally, the so-called addition energy that separates the electron levels in a QD is given by the sum of charging energy and single-particle level spacing:

$$E_{\text{add}} = E_{\text{C}} + \Delta \approx \frac{e^2}{C}. \tag{3.6}$$
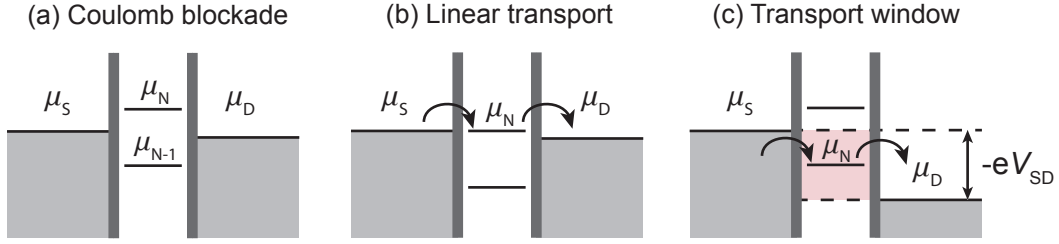
Figure 17: Energy level configurations corresponding to different transport regimes in a single dot.

In our system E_C clearly exceeds Δ, which can therefore be neglected for the ground state. The last energy scale to be considered is given by temperature as $k_B T$ and is roughly $10\,\mu eV$ in ou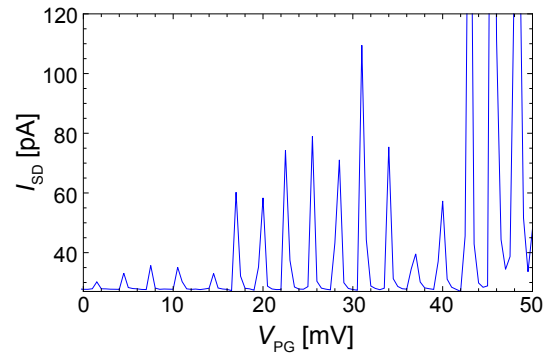r measurements. The relation between the different energies is essential for the observation of the Coulomb blockaded effect, which is introduced in the following.
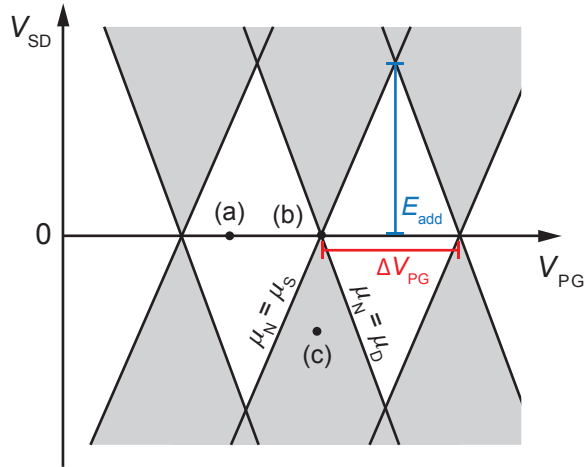
3.1.2   Coulomb blockade transport regime

Electron transport through quantum dots is limited by an effect known as the Coulomb blockade [12]. A measurement of the current I_{SD} through a quantum dot for a source-drain bias of $50\,\mu V$ as a function of PG voltage is presented in Fig. 16. It shows characteristic Coulomb peaks at certain plunger gate voltages V_{PG} and conduction is blocked for all other applied voltages. This phenomenon was named Coulomb blockade because it is rooted in the Coulomb repulsion between electrons in the dot. Coulomb blockade is the dominant effect if the Coulomb energy is the dominating energy scale. In particular, it must clearly exceed single-particle excitations. Additionally, the temperature needs to be sufficiently small and the tunneling coupling to the leads must be low as discussed in the previous section.

The energy configuration of the Coulomb blockade transport regime is illustrated in Fig. 17(a). The energy levels in the dot are filled up to electron $N-1$ and no further electron can be added to the dot, so that transport is blocked for zero source-drain bias. Transport can only occur if the chemical potentials μ_S and μ_D of source and drain, respectively, are aligned with a dot state. This is indicated by the arrows in Fig. 17(b). The dot levels are shifted by the the plunger gate, so that Coulomb peaks occur every time a dot level is aligned with μ_S and μ_D [19]. In the third configuration shown in Fig. 17(c) a source-drain bias V_{SD} is applied. A so-called transport window opens as the voltage

Figure 16: Measured Coulomb peaks in source-drain current against PG voltage. The peak shape is related to measurement resolution.

induces a difference between the chemical potentials of the leads. In this situation, current can flow for all plunger gate voltages for which an electron energy level is within the transport window and transport is blocked for all other V_{PG}.

Figure 18: Coulomb blockade diamonds of conductance through a single dot. The situations marked (a), (b) and (c) correspond to the energy level configurations presented in Fig. 17. Conductance occurs in the gray areas while transport is blocked in the white areas.

If the conductance is measured as a function of V_{PG} and V_{SD}, so called Coulomb diamonds are observed, as depicted in Fig. 18. Current flow is blocked in the white diamond shaped areas corresponding to transport situation (a) of Fig. 17. The conductance resonances along the line $V_{SD} = 0$ correspond to the Coulomb peaks originating from situation (b). The gray areas are associated with situation (c) where a dot state lies within the transport window, so that non-zero conductance is observed. Along each of the lines bordering the diamonds a dot state is aligned with either μ_S or μ_D, i.e. with the top or bottom of the bias window, as indicated in Fig. 18.

Two relevant parameters can be extracted from this diagram: the addition energy and the lever arm of the PG. The applied bias V_{SD} converts directly to the induced energy difference between the chemical potentials of source and drain (see Fig. 17(c)). For this reason, E_{add} (see Eq. (3.6)), which can here be approximated as the charging energy e^2/C, can directly be read from the diagram as indicated in blue. To convert the applied PG voltage to the energy shift of the dot levels a proportionality factor, the so-called lever arm, has to be introduced. It relates ΔV_{PG} (indicated in red in Fig. 18) and the addition energy as follows:

$$E_{add} = -|e|\alpha_{PG}\Delta V_{PG} \approx \frac{e^2}{C}. \tag{3.7}$$

The lever arm can therefore be extracted from the diagram as $\alpha_{PG} = |V_{SD}|/|\Delta V_{PG}|$. In a capacitance model, the lever arm is given by $\alpha_{PG} = C_{PG}/C$, where C is the total self capacitance of the dot [19]. A high lever arm is thus equivalent to a high capacitance of the PG.

3.2   Double quantum dots

Two quantum dots that are capacitively and tunneling coupled to each other via a tunneling barrier form a double quantum dot as depicted in Fig. 19. The relevant energy scales remain the same as in a single dot. However, in a double dot, additional quantities have to be taken into account, e.g. the capacitive and tunneling coupling between the two dots, which are given
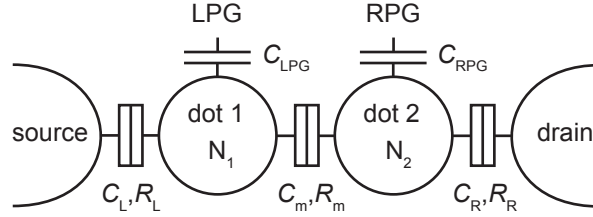
Figure 19: Schematic illustration of a double QD model. Each dot is capacitively coupled to a plunger gate and the two dots are tunneling coupled and capacitively coupled.

by C_{m} and R_{m}. In an accurate description, a finite cross coupling between the left plunger gate and right dot and vice versa have to be included, but they are neglected in the model that is illustrated in Fig. 19 and employed in the following. We only consider the capacitance between the left plunger gate (LPG) and dot 1 and between the right plunger gate (RPG) and dot 2.

In the following, linear and non-linear transport through double QDs are discussed. Stability diagrams are explained together with the relevant transport situations. In addition, the energies and capacitances characterizing the double dot system are presented as derived from a capacitor model. The section follows a review by van der Wiel et al. [16].
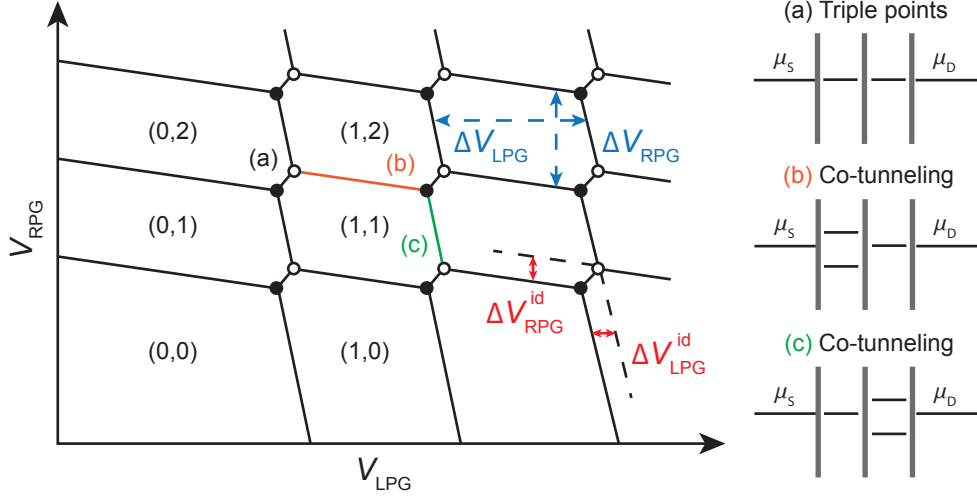
3.2.1 Stability diagram

The measurement of the conductance through a double dot as a function of both plunger gate voltages yields a so called stability diagram, which is schematically shown in Fig. 20. Conductance resonances form the hexagon pattern of the diagram. The region within each honeycomb cell corresponds to a certain fixed charge configuration of the double dot. The number of electrons in each dot is denoted by (N_1, N_2).

The depicted diagram holds for the linear conductance regime, in which a negligable bias voltage is applied between source and drain, $V_{\mathrm{SD}} \approx 0$. In this configuration, conductance peaks only occur when an electron level in both dots is aligned with the chemical potential of the leads as depicted in inset (a) of the figure. This condition is met at the triple points in the stability diagram ($\bullet, \circ$). The edges of the honeycomb cells originate from a co-tunneling process which is depicted in insets (b) and (c). Details about the co-tunneling regime can be found in [24, 25].

The voltage dimensions ΔV_{LPG} and ΔV_{RPG} marked in blue in the diagram are related to the charging energy of each of the two dots. If the inter-dot tunneling coupling is small, the separation of the triple points depends on strength of the capacitive inter-dot coupling. The dimensions $\Delta V_{\mathrm{LPG}}^{\mathrm{id}}$ and $\Delta V_{\mathrm{RPG}}^{\mathrm{id}}$ yield the so-called inter-dot coupling energy. These quantities are explained and derived on the basis of a capacitor model in section 3.2.2. A possible slanting of the honeycomb cells is due to capacitive cross coupling of the LPG and the right dot and vice versa.

A large tunneling coupling between the dots has the effect of a rounding of the hexagon outline near the triple points of the stability diagram as depicted in Fig. 21(a). The change in separation of the triple points quantifies the inter-dot tunneling coupling t, which is shown in red. However, the rounding can only be observed if t is sufficiently large compared to the other energy scales, especially temperature.

Figure 20: Schematic stability diagram in the linear transport regime. The charge configuration in each honeycomb cell is indicated in brackets. The transport situations corresponding to the triple points (a) and the lines marked (b) and (c) are illustrated on the right.

In the non-linear transport regime, i.e. when a finite source-drain bias is applied, the triple points expand into triangles. This is illustrated in an enlarged view of the triple points in Fig. 31. Again, the transport situations that apply at the corners of the triangles are displayed in the figure. The triangles expand with increasing bias and thus provide a means to extract the lever arms of the two PGs in the double dot configuration. The lever arms can be extracted with the help of the triangle dimensions $\delta V_{\text{L/RPG}}$. For a more thorough discussion of finite bias transport in double dots, the reader is referred to Refs. [16, 19].

3.2.2 Capacitor model

Like the single dot, the double dot system can be described by a capacitor model. With the help of this model, the characteristic electrostatic energies and capacitances of the system can be calculated from the voltage dimensions found in the transport measurements. The required formulas are presented in this section following Ref. [16].

The total capacitance $C_{1/2}$ of each dot in the double dot configuration can be found by considering all capacitances attached to it as connected in parallel, so that

$$C_{1/2} = C_{\text{L/R}} + C_{\text{L/RPG}} + C_{\text{m}}. \tag{3.8}$$

With this, the **charging energies** of the dots in the double dot configuration can be expressed as

$$E_{\text{C1}} = \frac{e^2}{C_1} \left(\frac{1}{1 - \frac{C_{\text{m}}^2}{C_1 C_2}} \right), \qquad E_{\text{C2}} = \frac{e^2}{C_2} \left(\frac{1}{1 - \frac{C_{\text{m}}^2}{C_1 C_2}} \right). \tag{3.9}$$

This corresponds to the single dot expression for the charging energy (3.3) corrected by a factor which accounts for the inter-dot coupling. This factor is usually small because $C_{\text{m}} \ll C_{1/2}$. In the coupled system, the energy of dot 1/2 does not only depend on $N_{1/2}$, but also on the number of charges on the other dot. The change in energy of one dot when an electron is
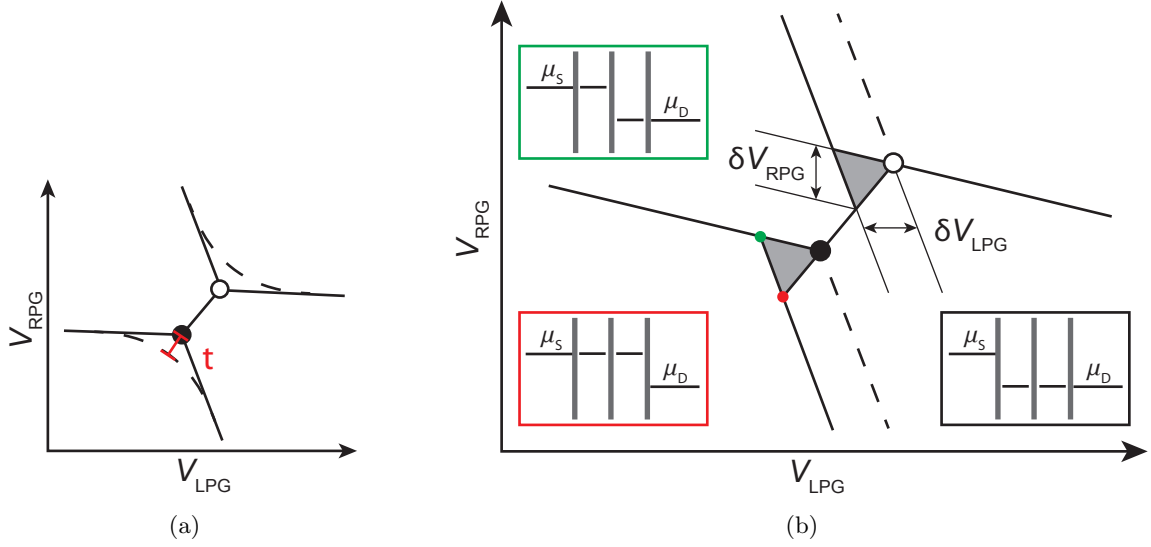
Figure 21: (a) Effect of inter-dot tunneling coupling on the stability diagram near the triple points. (b) Finite bias triangles evolving at the triple points in the non-linear transport regime. The depicted energy configurations occur at the corners of the triangle.

added to the other dot is called **inter-dot charging energy** or **coupling energy** and it is given by

$$E_{\mathrm{Cm}} = \frac{e^2}{C_{\mathrm{m}}} \left(\frac{1}{\frac{C_1 C_2}{C_{\mathrm{m}}^2} - 1} \right) \tag{3.10}$$

These energies and all capacitances of the system can be calculated using the information obtained from measured stability diagrams. The dimensions $\Delta V_{\mathrm{L/RPG}}$ and $\Delta V_{\mathrm{L/RPG}}^{\mathrm{id}}$ indicated in Fig. 20 are related to the capacitaces of system through the following equations:

$$\Delta V_{\mathrm{L/RPG}} = \frac{|e|}{C_{\mathrm{L/RPG}}}, \tag{3.11}$$

$$\Delta V_{\mathrm{L/RPG}}^{\mathrm{id}} = \frac{|e|C_{\mathrm{m}}}{C_{\mathrm{L/RPG}}C_{1/2}}. \tag{3.12}$$

The lever arms of the plunger gates in the double dot configuration differ from those in each individual dot and can only be obtained from finite bias triangles. They are given by

$$\alpha_{\mathrm{L/RPG}} = \frac{C_{\mathrm{L/RPG}}}{C_1} = \frac{|V_{\mathrm{SD}}|}{\delta V_{\mathrm{L/RPG}}} \tag{3.13}$$

Combining equations (3.11), (3.12) and (3.13), we can find the values of the capacitances C_1, C_2 and C_{m}. This is sufficient to calculate the charging energies and the coupling energy. These quantities together with the inter-dot tunneling coupling characterize the double quantum dot system.
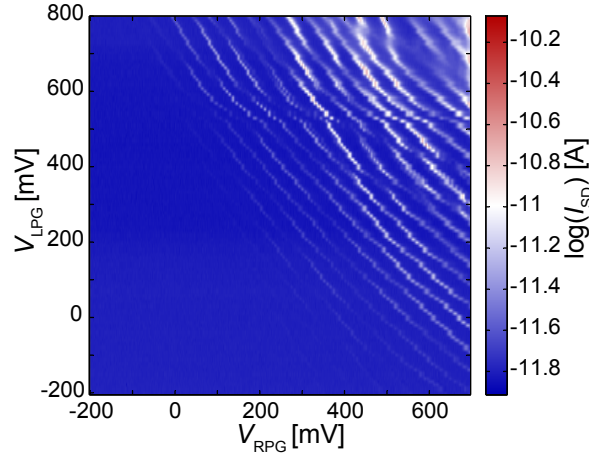
Figure 22: Stability diagram measured with a direct current signal. For negative PG voltages the signal is lost.

3.3   Quantum point contacts as charge detectors

Stability diagrams can be recorded by measuring the direct current through the double quantum dot. An example measurement using this signal is presented in Fig. 22, where the source-drain current is plotted on a logarithmic scale. For negative PG voltages the dots are successively emptied of electrons. It can be observed that in this region t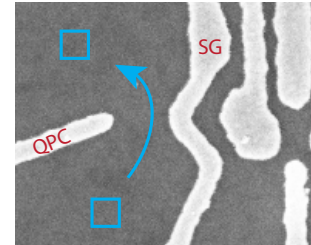he current signal is lost. A solution that enables few electron measurements is presented by a quantum point contact (QPC) charge detector. Field et al. [26] first implemented a QPC to measure the occupation sequence of a quantum dot.

The QPC in our system is a narrow constriction in the two-dimensional electron gas in the vicinity of the quantum dot, which is realized by top gates as shown in Fig. 23. The constriction is formed by a side gate (SG) and a QPC gate and its width can be controlled by the applied gate voltages. The QPC is separated from the dot structure, so that it is not tunnel coupled to the dot. A charge detector bias V_{CD} is applied via Ohmic contacts to the 2DEG (shown in blue). The conductance through the QPC is quantized, which can be exploited to achieve a high sensitivity of the QPC conductance to potential changes in the quantum dot [19]. Each change in

Figure 23: QPC top gate structure. Ohmic contacts to the 2DEG are shown in blue.

charge configuration of the double dot means a potential change and can be observed in the conductance through the QPC. The occupation of the QD can thus be measured with a QPC charge detector (CD).

In the first two plots of Fig. 24 the measurement signal of the current through a single dot and the charge detector current are plotted against V_{RPG}. For more negative RPG voltages the right dot is emptied. Each tunneling process of an electron is seen as a resonance in I_{SD}. Each step in the CD current signal also corresponds to a quantized change of charge on the quantum dot. For negative PG voltages the dot current is not measurable anymore. The CD, on the contrary, is sensitive down to single electrons as long as the background is suitably configured.
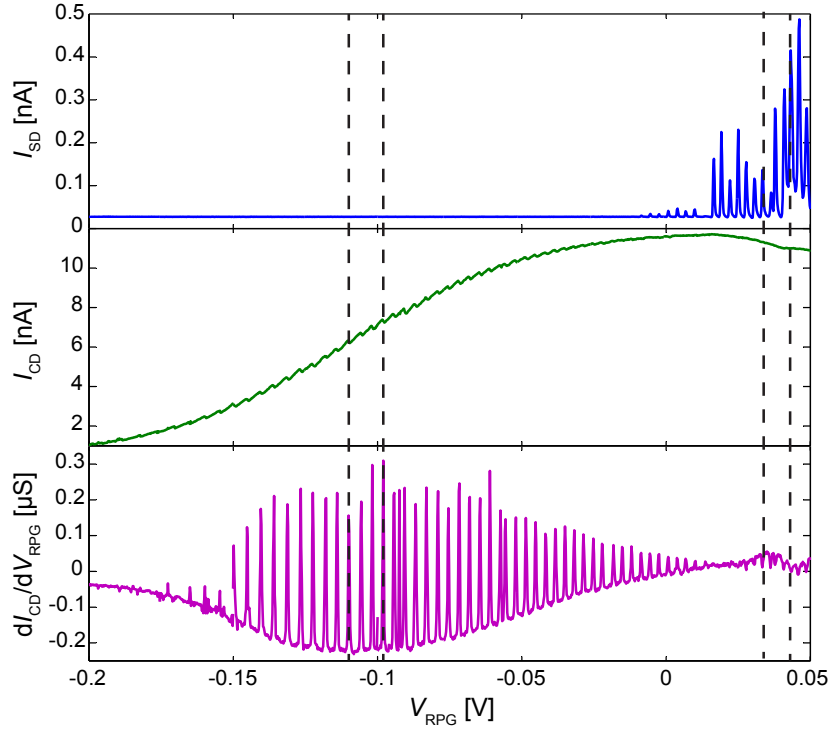
Figure 24: Comparison of different measurement signals. At the top, the direct source-drain current through the dot is plotted against PG voltage. The middle plot shows the current through the CD and the bottom plot the transconductance of the CD against V_{RPG}.

The CD signal can be enhanced by considering the differential conductance $\mathrm{d}I_{\mathrm{QPC}}/\mathrm{d}V_{\mathrm{PG}}$. Because the numerical derivative introduces additional noise it is preferable to measure the transconductance of the QPC instead. A constant amplitude AC modulation $\mathrm{d}V_{\mathrm{PG}}$ is added to V_{PG} and the resulting modulation of the charge detector current $\mathrm{d}I_{\mathrm{CD}}$ is measured with a lock-in technique. The transconductance is given by

$$\frac{\mathrm{d}I_{\mathrm{CD}}}{\mathrm{d}V_{\mathrm{PG}}}. \tag{3.14}$$

This signal is shown in purple in Fig. 24. Each peak corresponds to a change in dot occupation and occurs at exactly the same PG voltages as the steps in the current signal.

4   Quantum Dot Measurements

The main work performed for this thesis was the characterization of new quantum dot designs for measurements in the few electron regime. This section first treats the QD samples. Sample fabrication and the different tested designs are discussed together with the relevant design considerations. The characterization of three tested samples in the few electron regime is presented next. A particular problem that became apparent in the characterization measurements was related to the inter-dot tunneling coupling. Measurements investigating this problem are presented in the last part of the section.

4.1   Sample design

The chip setup of the microwave samples, which are used for the qubit-resonator coupling experiments were presented in section 1. In the course of this thesis new quantum dot sample designs were developed and characterized by DC transport measurements. For these measurements, the QD samples were not integrated in a resonator chip and had a slightly different geometry than the QD designs for RF measurements that were introduced in Fig. 4.

In the DC samples, ten top gates were used to control the double quantum dot and two quantum point contacts. A scanning electron microscope (SEM) image of one of the tested sample geometries is shown in Fig. 25. The abbreviated names of the top gates are indicated in red. The double dot is formed between the left and right side gate (LSG and RSG), where the center gate (CG) and the source drain barrier (SDB) form the central tunneling barrier between the two dots. Two plunger gates (LPG and RPG) extend over the left and right dot. In the microwave samples, the resonator gate simultaneously functions as one of these PGs. Next to the SDB the left and right drain barrier (LDB and RDB) are used to open or close the gap to the side gates in a controlled fashion. The ohmic contacts to the 2DEG are indicated by the colored squares. Transport through the double dot can be induced by applying a bias between the source (S) and drain (D) contacts shown in orange.

To the left and right of the double dot structure, two quantum point contacts are positioned to be operated as charge detectors. The blue ohmic contacts can be biased to generate a QPC current. The QPC structures are well separated from the double QD, so that electrons cannot tunnel between the systems. Each of the QPCs can be operated as charge detector for both quantum dots.

In this section, the sample fabrication is briefly summarized first. Various different sample designs had to be characterized in the course of finding the most suitable geometry for our application. These samples are presented in the second part together with the considerations leading to the particular designs.

4.1.1   Fabrication

Our laterally defined quantum dot was realized on a $GaAs/Al_xGa_{1-x}As$ wafer with a 2DEG at the interface of the heterostructure about 90 nm below the surface. This type of wafer was thoroughly characterized in section 2. The samples were fabricated in three photo lithography and one electron beam (e-beam) lithography step. First, the mesa structure holding the 2DEG was etched. Second, the ohmic contacts, formed by a Ge, Au, Ge, Au, Ni, Au metal sequence, were defined by photo lithography, vapor deposited on the wafer and annealed to contact the 2DEG. The Ti/Au leads to the top gates were also fabricated by photo lithography, while
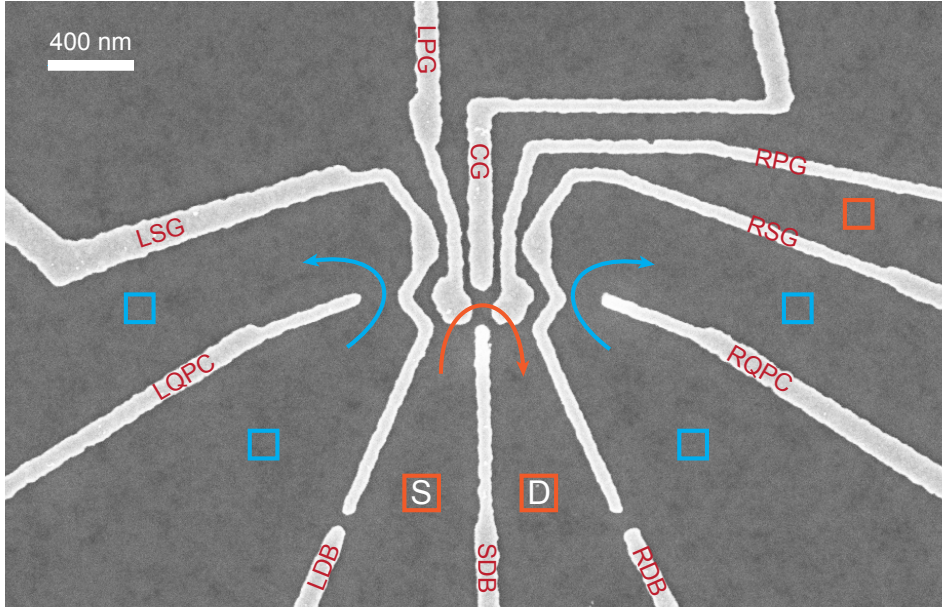
Figure 25: SEM image of an exemplary sample. From top to bottom the center gate (CG), left and right plunger gate (LPG/RPG), left and right side gate (LSG/RSG), left and right quantum point contact (LQPC/RQPC), left and right drain barrier (LDB/RDB) and source drain barrier (SDB) are indicated. The functions of the various top gates are explained in the text. The squares represent the ohmic contacts to the 2DEG. The double dot is connected to a source (S) and drain (D) contact (shown in orange) and transport through each of the QPCs can be induced with the blue ohmic contacts.

their fine structure was defined by e-beam lithography. For the top gate fine structure a bilayer of 3 nm Ti and 25 nm Au was deposited.

4.1.2 Design considerations and different geometries

With the quantum dots characterized in this thesis, several improvements were intended with respect to previous designs. In this section, the different requirements that the new samples need to fulfill are explained chronologically following the evolution of our sample designs. All sample geometries that were realized are introduced and the improvements between each sample generation are highlighted. Here and in the following, they are numbered chronologically for distinction starting with sample 05.

As discussed in section 1.3, the new designs were planned for operation with only few electrons per dot. This eliminates any problems related to excited states in many electron dots, which are closely spaced in energy. One conclusion regarding the dot design is that the electrons should not be confined to the dot by a mesa edge as this might complicate the process of emptying the dots. Therefore, in the new designs, the dots are formed using only top gates. This consideration was realized in sample design 05, which is shown in Fig. 26: no mesa edge is needed to form the dots. Additionally, two QPC charge detectors are included, which are used for few electron transport measurements as explained in section 3.3. The plunger gates of this sample do not extend over the dot area and therefore have a low capacitance.

The size and shape of the plunger gates play a particularly important role for our QD

designs. The over-all goal of the project is to reach strong coupling, which can only be achieved if the decoherence and decay rates of qubit and resonator are small compared to the coupling strength g. It is therefore the objective to maximize the coupling strength g. The resonator-dot coupling strongly depends on the capacitance C_{RG} between the resonator gate and the quantum dot to which it extends [9]:

$$g \propto \frac{C_{\text{RG}}}{C_{\text{RG}} + C_{\text{g}}}. \tag{4.1}$$

In this equation, C_{g} is the capacitance of the whole quantum dot system to ground. The cross coupling of the RG respectively PG to the second dot as well as the capacitance C_{g}, which also depends on C_{RG}, cannot be easily determined in our system. Therefore, the relation (4.1) only provides us with an upper bound for the increase of the coupling strength with C_{RG}: if C_{RG} is increased by a factor x, g cannot be increased by more than a factor x.

The obvious way to increase the capacitance of the resonator gate is to enlarge its area, which was implemented in designs 06s and 06a (see Fig. 26). In the symmetric sample 06s, the two plunger gates cover most of the dot area, from which a large plunger gate capacitance is expected. The second design 06a is asymmetric in the two dots, with only one extended plunger gate, which is planned as the resonator gate. Extended plunger gates have the additional advantage that they make it easier to empty the dots as negative voltages can be applied directly above the dot area.

Another aspect that needs to be kept in mind is that the microwave experiments with the resonator require tunneling coupling of the two dots. This becomes apparent in the Jaynes-Cummings interaction of the double dot and the resonator, which depends on the tunneling coupling t between the dots [9, 1]. In our measurements of sample 06s, it was found that a high tunneling coupling between the dots and large plunger gate capacitances can be competing goals in few electron measurements. The plunger gates can strongly influence the tunneling barrier between the dots and can thereby diminish the tunneling coupling. This is discussed in detail in section 4.3.

This result was taken into account for the design of the symmetric and asymmetric samples 07s and 07a, respectively (see Fig 26(d) and (e)). They have smaller plunger gates than the samples 06, which do not come as close to the central barrier between the two dots. This is expected to improve the tunneling coupling.

After the characterization of the samples 07, the design was further improved. The designs 09 shown in Fig. 26(f) and (g) are currently thought to be most promising. The plunger gates are removed even further from the central barrier. Additionally, the designed distance between the CG and the SDB was increased from $165\,\text{nm}$ in designs 05 through 07 to roughly $200\,\text{nm}$ in the designs 09. The SDB was also slightly moved upward with the result that the QPCs connecting the dot to source and drain and the central QPC are more similar in width. These changes are hoped to facilitate a symmetric tuning of the barriers and increase the tunneling coupling between the dots.

Many different aspects need to be taken into account for a sample design that fulfills the different, partly competing requirements of the intended microwave measurements. The characterization measurements performed for this thesis had the goal to develop an optimized sample design that unites all of the discussed considerations. Due to problems with the sample lifetime only the symmetric samples 05, 06s and 07s could be characterized at very low temperature. The samples were very easily damaged by electrostatic discharge. The obtained measurement results are presented and discussed in the following section.
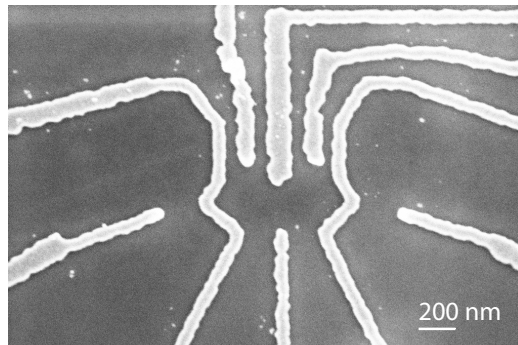
(a) Design 05
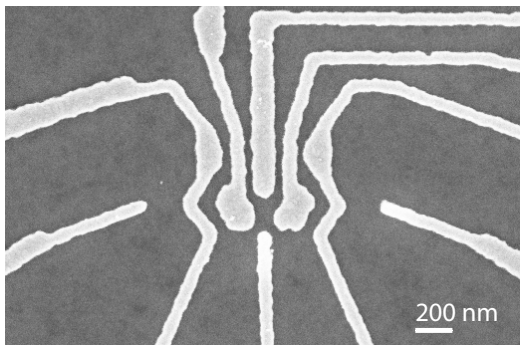
(b) Design 06s
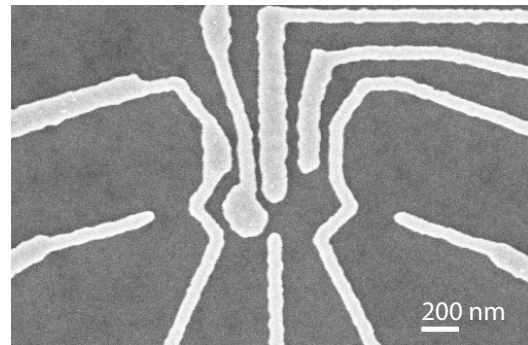
(c) Design 06a
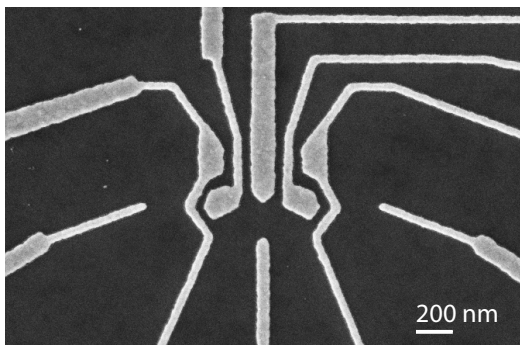
(d) Design 07s
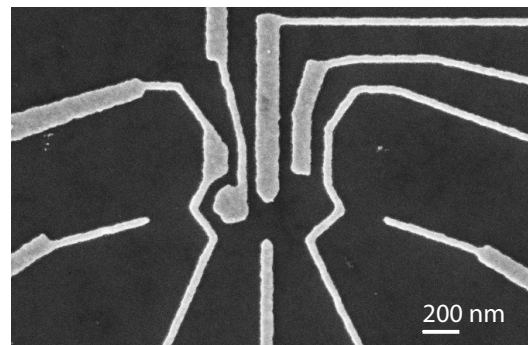
(e) Design 07a
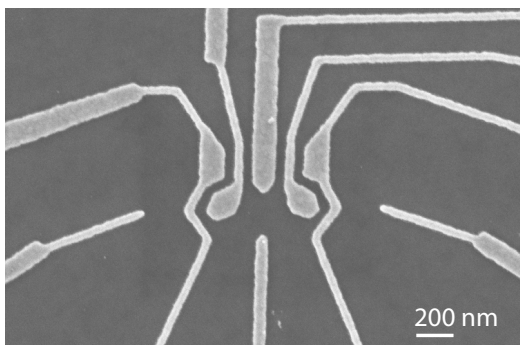
(f) Design 09s
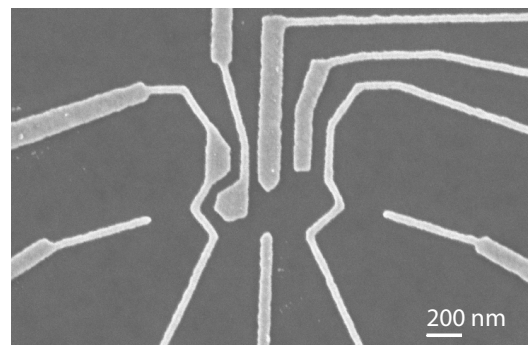
(g) Design 09a

Figure 26: SEM images of the realized sample geometries. The differences are discussed in the text. Only samples 05, 06s and 07s were characterized at low temperature.

34

4.2   Transport measurements in the few electron regime

In order to fully characterize the tested samples, it was the goal to extract all relevant sample properties such as charging energies and lever arms from transport measurements. Because the samples were designed for operation in the few electron regime, measurements in this regime are most interesting for the sample characterization. For this reason, mainly data that was acquired in measurements in the few electron regime is presented and discussed in the following.

The many electron sample design that was presented in Fig. 4(a) serves as a reference to which any extracted sample properties have to be compared. This sample was employed in the previously published experiments [1, 15]. For convenience it will be referred to as sample 00 in the following. For this sample, the resonator gate had a lever arm of $\alpha_{\mathrm{RG}} = 0.6$. It must be taken into account, however, that a different wafer structure with a 35 nm deep 2DEG was used for sample 00. In our samples the 2DEG was 90 nm deep, so that the capacitance and therefore also the lever arm of the gates is expected to be roughly a factor of 3 lower for the same sample geometry. The 90 nm wafer was chosen because it is difficult to fabricate few electron QDs on shallow 2DEG wafers due to limitations in the lithographic resolution. The inter-dot coupling energy was $E_{\mathrm{C,m}} \approx 0.2$ meV and the inter-dot capacitance was $C_{\mathrm{m}} \approx 4$ aF.

The transport experiments were performed in a dilution refrigerator with a base temperature of approximately 20 mK. The source drain bias as well as the bias of the charge detectors were applied symmetrically. For this purpose and for measuring the dot and QPC currents, symmetrical double I-V converters were used.

4.2.1   Design 05

The first sample to be measured had the design 05 (see Fig. 26(a)). During cool-down, a pre-bias of $+0.3$ V was applied to all gates. This results in a decreased density of ionized donors below the gated areas when the pre-bias is turned off at low temperature and creates an effective negative potential [27]. Consequently, less negative bias needs to be applied in order to deplete below the top gates. Fig. 27 shows Coulomb diamond measurements of the left and right single quantum dot. The source drain bias V_{SD} was swept for a wide range of left and right plunger gate voltages. The numerical derivative of the direct current through the quantum dot with respect to the source drain bias, $\mathrm{d}I_{\mathrm{SD}}/\mathrm{d}V_{\mathrm{SD}}$ is plotted on the logarithmic scale. The measurements were performed in a voltage regime with many electrons in the dot.

From this data, the lever arms of the two plunger gates were extracted to be $\alpha_{\mathrm{LPG}} \approx 0.022$ and $\alpha_{\mathrm{RPG}} \approx 0.020$. The charging energies of the left and right dot could also be determined from the marked diamonds as $E_{\mathrm{C,L}} \approx 2.35$ meV (568 GHz) and $E_{\mathrm{C,R}} \approx 2.33$ meV (563 GHz). The well pronounced lines outside the diamonds in both measurements shown in Fig. 27 originate from excited states. The energy spacing between the observed excited states can be extracted as roughly 0.4 meV or smaller in both dots.

The design was next tested as a double quantum dot. The double dot was successfully operated in the few electron regime as demonstrated by the stability diagram shown in Fig. 28. The plot shows the transconductance of the left charge detector, where V_{RPG} was modulated, in a 2D map of left vs. right PG voltage. The charge configurations corresponding to the honeycomb cells of the stability diagram are indicated in parentheses by the number of electrons in each dot: (N_1, N_2). From the fact that no more lines, respectively transconductance peaks, appear for more negative gate voltages, it can be concluded that both dots are
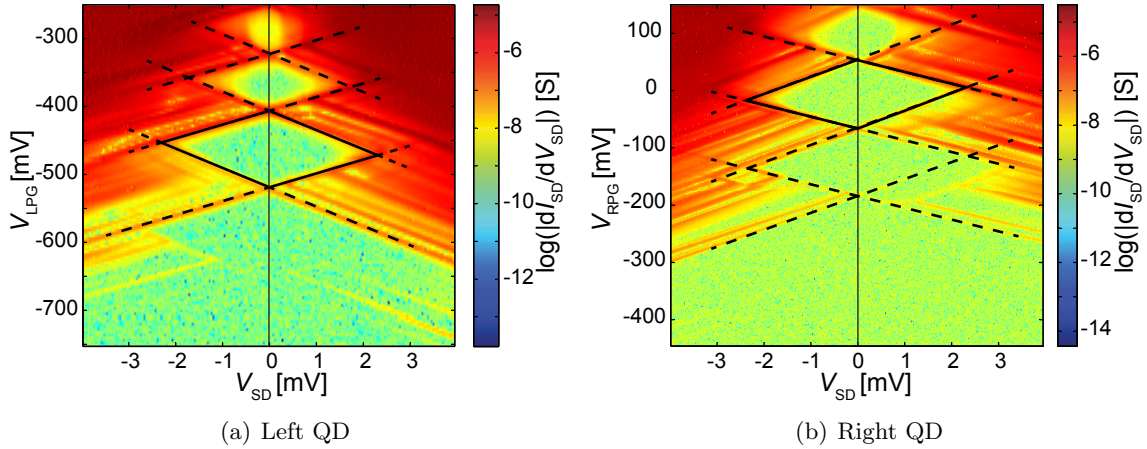
Figure 27: Coulomb diamond measurements of the left and right single dots of sample 05 in the many electron regime. Excited states are clearly visible.

emptied in the area marked by (0, 0) in the plot.

This measurement allows the extraction of the voltage differences $\Delta V_{\mathrm{RPG}} \approx 181\,\mathrm{mV}$ and $\Delta V_{\mathrm{LPG}} \approx 165\,\mathrm{mV}$, which are proportional to the charging energies of the two dots. A zoom around the triple points connecting the (0,0) and (1,1) honeycomb cells as shown in Fig. 28(b) yields information about the capacitive inter-dot coupling. From the voltage differences $\Delta V_{\mathrm{LPG}}^{\mathrm{id}} \approx 10.5\,\mathrm{mV}$ and $\Delta V_{\mathrm{RPG}}^{\mathrm{id}} \approx 11.3\,\mathrm{mV}$, the inter-dot charging energy can be calculated using the lever arms of the plunger gates.

The exact lever arms of the two plunger gates in the double dot configuration can only be extracted from finite bias triangles. In the attempt of finite bias triangle measurements, we increased V_{SD} from 100 to 400 μV. The single dot lever arms found above can be used to find an estimate of the expected dimensions of the triangles at the applied bias according to Eq. (3.13). This estimation yields voltage dimension of the triangles of roughly 20 mV, which would easily be observable on the scale of the measurement in Fig. 28(b). Nevertheless, we could not observe triangles for any of the tried bias settings.

This behavior was unexpected and could have various reasons, some of which are discussed in section 4.3. It is possible that a careful fine tuning of the central tunneling barrier between the two dots or other gates might have helped to resolve finite bias triangles. The reason for this is that finite bias triangles only develop if there is transport through the double dot, which requires a finite tunneling coupling between the dots. Unfortunately, this sample broke in a second cool-down before these options could be explored.

The relevant sample parameters could only be estimated using the plunger gate lever arms of the single dot configuration because the finite bias triangle measurements were not successful. These calculations yield the charging energies $E_{\mathrm{C,L}} \approx 4.0\,\mathrm{meV}$ (967 GHz) and $E_{\mathrm{C,R}} \approx 3.3\,\mathrm{meV}$ (801 GHz) for the left and right dot in the double dot configuration. The fact that these energies are higher than in the single dot configuration can largely be attributed to the fact that they were extracted from measurements in the few electron regime, which generally yield higher charging energies. Of course, these energies cannot be directly compared as they are expected to differ from the single to the double dot configuration. Again, using the approximate lever arms, the inter-dot coupling energy is calculated to be $E_{\mathrm{C,m}} \approx 0.23\,\mathrm{meV}$ (56 GHz). The capacitance between the two dots additionally quantifies the capacitive inter-

(a)

(b)
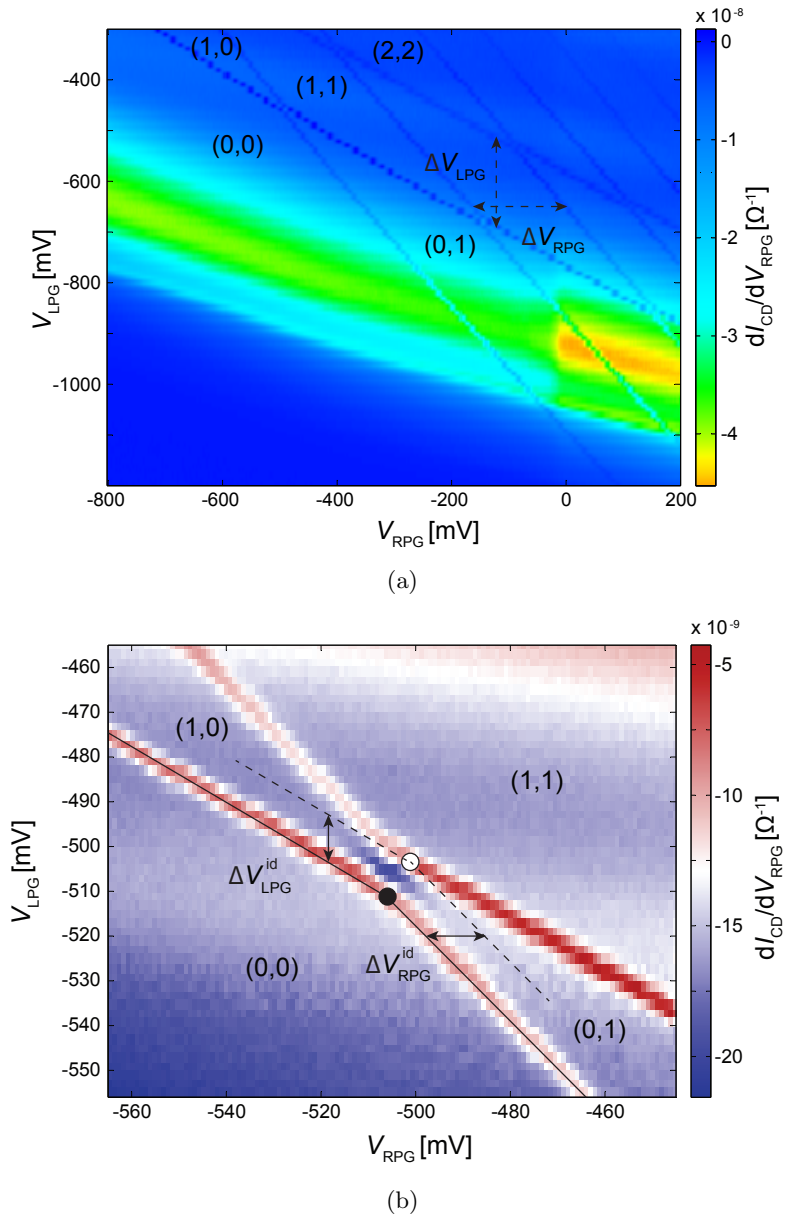
Figure 28: Double QD stability diagrams of sample 05 in the few electron regime. The extracted voltage dimensions are indicated.
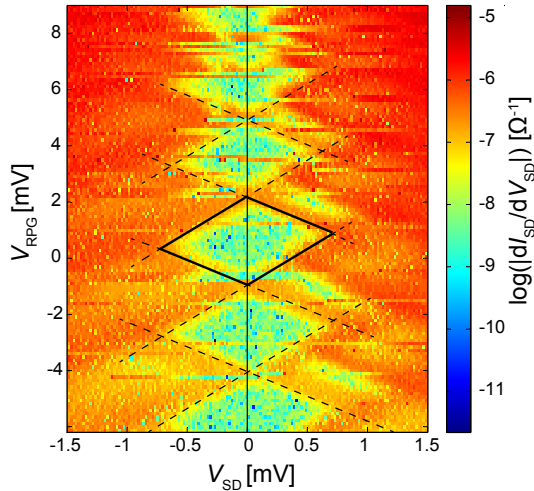
Figure 29: Coulomb diamond measurement of the right dot of sample 06s in the many electron regime.

dot coupling: $C_{\mathrm{m}} \approx 2.8\,\mathrm{aF}$.

Keeping in mind the ultimate application of the QD samples in the resonator setup, the lever arm of the resonator gate is the most important sample parameter. With values around 0.02, the plunger gate lever arms are very low for this sample design compared to $\alpha_{\mathrm{RG}} \approx 0.6$ for sample 00. The capacitive inter-dot coupling can be quantified as intermediate as it is comparable to that in sample 00. From the comparison of the lever arms of samples 05 and 00, an upper limit for the resonator-dot coupling strength in sample 05 can be estimated using to Eq. (4.1): $g/2\pi \leq 2\,\mathrm{MHz}$.

4.2.2   Design 06

In order to achieve a higher lever arm, the samples 06 were designed to have extended plunger gates. The symmetric design 06s, which was shown in Fig. 26(b), was tested at low temperature. A pre-bias of $+0.3\,\mathrm{V}$ was applied to all top gates excluding the plunger gates for the cool-down. In this design, the PGs cover the dot area in which a pre-bias would be disadvantageous for the transport measurements as it would create a depleting potential.

For this sample, only the right dot was measured as a single dot. The resulting Coulomb diamond measurement is presented in Fig. 29. Again, the numerical derivative of the current through the dot is plotted on a logarithmic scale. The gate voltage was stepped between roughly $+9\,\mathrm{mV}$ and $-5\,\mathrm{mV}$. In this voltage regime a very large number of electrons is expected in the quantum dot. The data also shows many charge rearrangements especially for positive gate voltages. This agrees with the experience from previous experiments that the samples are less stable for positive applied gate voltages. From the diamond framed in black, the lever arm of the RPG and the charging energy of the right dot were extracted to be $\alpha_{\mathrm{RPG}} \approx 0.24$ and $E_{\mathrm{C,R}} \approx 0.71\,\mathrm{meV}$.

Like for design 05, both dots could be emptied without complications. A few electron measurement of the double dot is presented in Fig. 30(a). The transconductance of the right charge detector was measured for a modulated voltage of the left plunger gate. Careful
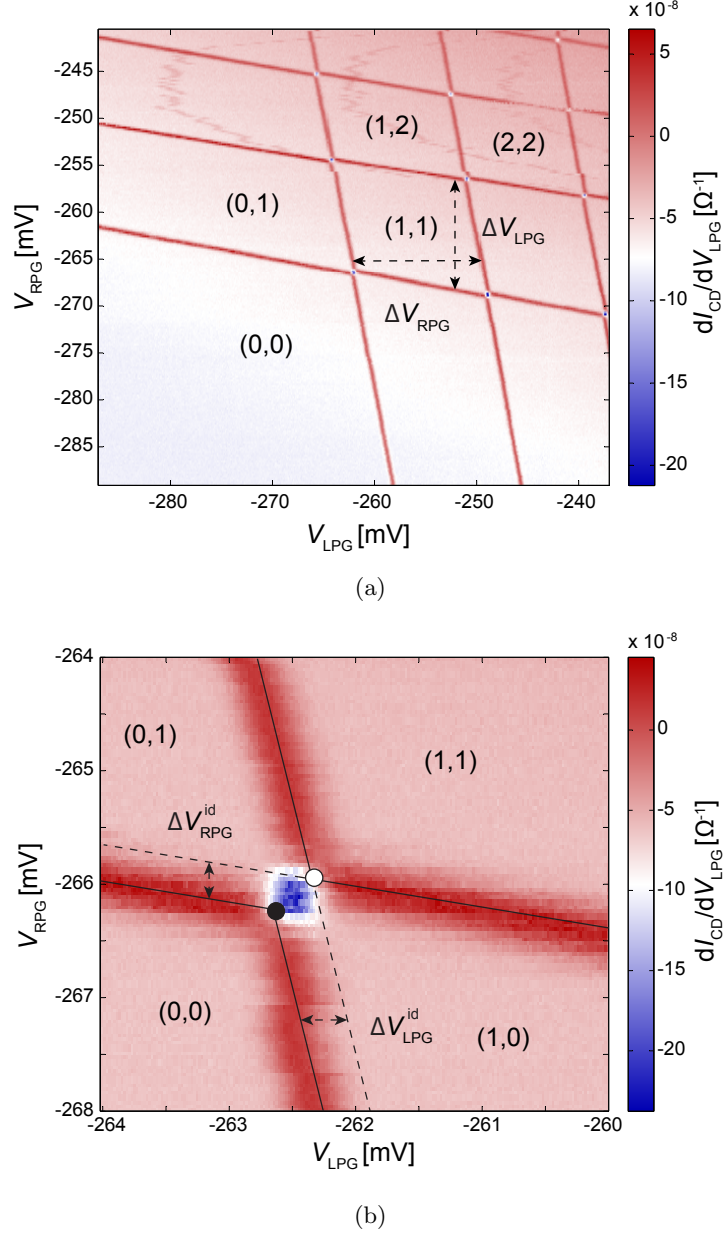
Figure 30: Double QD stability diagrams of sample 06s in the few electron regime. The extracted voltage dimensions are indicated.

additional measurements confirmed the double dot charge configurations that are assigned to the cells in the figure. A zoom-in around two of the triple points is shown in Fig. 30(b). The relevant voltage dimensions in these plots are given by $\Delta V_{\mathrm{LPG}} \approx 12\,\mathrm{mV}$, $\Delta V_{\mathrm{RPG}} \approx 13\,\mathrm{mV}$, $\Delta V_{\mathrm{LPG}}^{\mathrm{id}} \approx 0.37\,\mathrm{mV}$ and $\Delta V_{\mathrm{RPG}}^{\mathrm{id}} \approx 0.32\,\mathrm{mV}$.

For this sample it was again impossible to resolve finite bias triangles. We applied a maximal source drain bias of $200\,\mu\mathrm{V}$, from which we would expect triangle dimensions of $1\,\mathrm{mV}$ inserting the single dot lever arm. For this sample, we tried to open the central barrier by carefully increasing the center gate voltage V_{CG} from -980 mV to -290 mV. The hope was
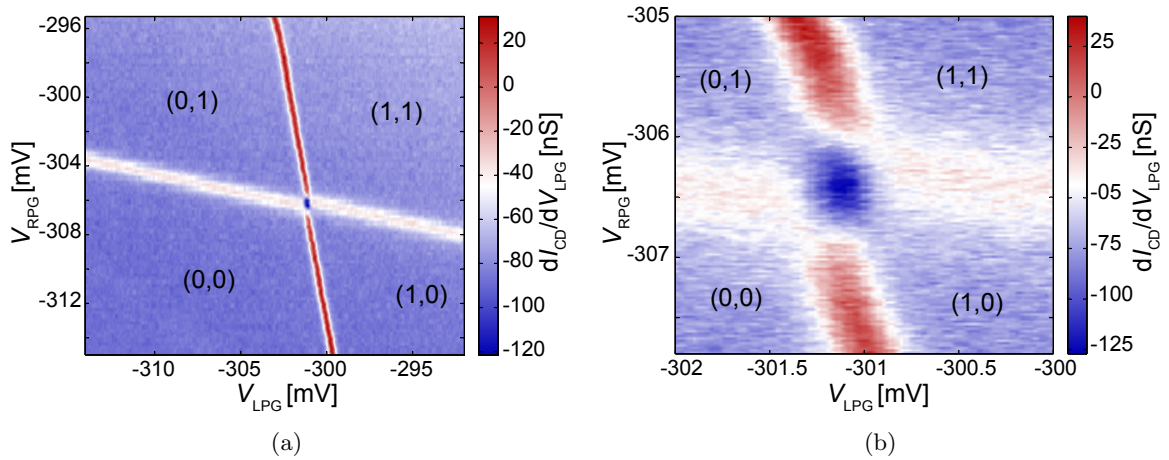
Figure 31: Zoom-ins around triple points of a stability diagram of sample 06s for $V_{CG} = -400\,\text{mV}$.

that this would lead to the appearance of finite bias triangles by increasing the inter-dot tunneling coupling. They could not be observed for any of the settings, however. This result is further discussed in section 4.3.

A measurement with the setting $V_{CG} = -400\,\text{mV}$ is shown in Fig. 31. Opening the central barrier is expected to increase the tunneling coupling between the dots, which would result in a rounding of the triple point corners as described in section 3. This would increase the distance between the triple points in the presented measurements. This effect cannot be observed, however, as the distance between the triple points is roughly the same as in Fig. 30(b) when projected on the LPG and RPG voltage axes. From this we can conclude that the slight rounding that is visible in the data is not due to tunneling coupling but rather due to temperature broadening, which is not unexpected. The electronic temperature of our samples is roughly $T_e \approx 130\,\text{mK}$, which yields an energy of $k_B T_e \approx 11\,\mu\text{eV}$ (3 GHz). Even for the setting $V_{CG} = -400\,\text{mV}$, the tunneling coupling between the dots is therefore below $11\,\mu\text{eV}$.

Because finite bias double dot measurements did not yield results, the properties of sample design 06s had to be extracted inserting the single dot lever arm of the RPG instead of both double dot lever arms. The resulting charging energies are $E_{C,L} \approx 2.9\,\text{meV}$ (697 GHz) and $E_{C,R} \approx 3.1\,\text{meV}$ (755 GHz). The inter-dot charging energy is $E_{C,m} \approx 0.1\,\text{meV}$ (21 GHz), which is about half as big as what was observed for sample 05. Reason for the decreased charging energies is the increased PG capacitance in sample 06s, which contributes to higher total capacitances $C_{1/2}$. The reason for this is the increased Correspondingly, the inter-dot capacitance is also reduced: $C_m \approx 1.6\,\text{aF}$.

In summary, the lever arm of this sample, $\alpha_{RPG} \approx 0.24$, was more than a factor 10 higher than that of the design without extended plunger gates. This positive result is expected from the sample geometry that would suggest a much higher PG capacitance. The lever arm of sample 06s is approximately a factor of 3 lower than that of sample 00, which accounts for the lower depth of the 2DEG in sample 00. As an upper bound for the resonator-dot coupling strength, we find $g/2\pi \leq 20\,\text{MHz}$. The capacitive inter-dot coupling was reduced by roughly a factor of two, however. The presented data does not allow a definite conclusion about the tunneling coupling as the relevant quantity for our purposes. Nevertheless, the problems to observe finite bias triangles lead to the question whether the two dots were sufficiently
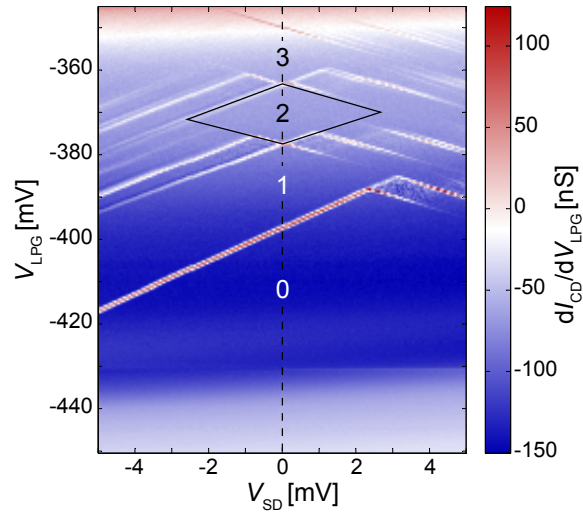
Figure 32: Coulomb diamond measurement of the left dot of sample 07s in the few electron regime. The electron numbers corresponding to each diamond are indicated.

strongly coupled to each other.

4.2.3 Design 07

For the tested sample with design 07s only the left QD could be operated, unfortunately, because the right side gate was defective. Again, a pre-bias of $+0.3\,\mathrm{V}$ was applied to all top gates except the PGs. An SEM image of the sample is shown in Fig. 26(d).

The left dot, which could be formed with the remaining gates, was studied thoroughly to extract as much information about the sample as possible with single dot measurements. Coulomb diamond measurements were therefore not only performed in the many electron regime, but also in the few electron regime. One of these measurements is presented in Fig. 32, in which the transconductance of the left charge detector is plotted. From the marked diamond a lever arm $\alpha_{\mathrm{LPG}} \approx 0.17$ and a charging energy $E_{\mathrm{C,L}} \approx 2.3\,\mathrm{mV}$ can be extracted. This lever arm yields $g/2\pi \leq 15\,\mathrm{MHz}$ as upper bound of the coupling strength. The number of electrons in the dot for the different PG voltage settings is indicated in the plot. Only for the diamond corresponding to two electrons in the dot all bordering lines are clearly visible. The reason for this is discussed in section 4.3.

In the presented data, lines originating from excited dot states are very pronounced. The energy spacing between the ground state with one electron in the dot ($\mu_1^{(0)}$) and the first excited state ($\mu_1^{(1)}$) can be extracted to be $\mu_1^{(1)}$- $\mu_1^{(0)} \approx 2.3\,\mathrm{meV}$ (556 GHz). For comparison, the energy difference between the one and two electron ground states is $\mu_2^{(0)}$- $\mu_1^{(0)} \approx 3.2\,\mathrm{meV}$ (774 GHz). The excited states corresponding to two electrons in the dot yield $\mu_2^{(1)}$- $\mu_2^{(0)} \approx 0.9\,\mathrm{meV}$ (217 GHz) and $\mu_2^{(2)}$- $\mu_2^{(0)} \approx 1.9\,\mathrm{meV}$ (459 GHz). These excited states can be identified as singlet ($\mu_2^{(1)}$) and triplet ($\mu_2^{(2)}$) states [19]. The extracted spacings between the ground and excited states are on the order of magnitude of the charging energy of the dot and are therefore much higher than $k_{\mathrm{B}}T$ or the resonance frequency of the resonator $f_0 \approx 6.8\,\mathrm{GHz}$,

which is desired for microwave experiments. Compared to the excited states observed in the many electron Coulomb diamond measurements of sample 05 (see Fig. 27) the spacing is significantly increased. This shows that the single-particle level spacing is indeed much larger in dots in the few electron configuration than in many electron dots.

The observed properties of all samples corresponded well to what was expected from sample geometry. The extracted lever arm of the left plunger gate is 0.17, which is about 30% lower than that of sample 06s. This is in agreement with the reduced area of the PGs. It is still by a factor of 8 higher than the lever arms of the short PGs of sample 05, however. The capacitive inter-dot coupling can only be compared for samples 05 and 06s. Both, the inter-dot coupling energy $E_{C,m}$ and capacitance C_m were reduced by about half for sample 06s.

The relevant quantity for our experiments is the tunneling coupling, however. This cannot be directly deduced from the presented measurement data. It is the aim of the following section to motivate conclusions about this quantity. All other relevant capacitances of the characterized double dot systems were also calculated and are summarized in appendix A, where all sample properties are listed in a table for convenient comparison.

4.3   Investigation of inter-dot tunneling coupling

All tested dot designs could successfully be emptied and measured in the few electron regime. In this respect, the new sample designs represent a significant improvement with respect to the previous designs. The samples must, however, also fulfill the other requirements of the resonator experiments for which they are intended, one of which is tunneling coupling between the dots in the GHz range.

The tunneling coupling cannot be directly quantified based on our data because it is energetically smaller than temperature broadening as illustrated in section 4.2.2. However, the fact that it was impossible to resolve finite bias triangles for both samples 05 and 06s raises the question whether the dots were sufficiently tunneling coupled.

The signal recorded in our measurements is the transconductance of a charge detector, which measures the change in occupation. Finite bias triangles can be resolved with this signal under two conditions: the barriers to the leads as well as the central barrier must allow tunneling and all barriers need to be configured in a way that transported electrons remain in the dots long enough to be registered by the detector. Finite bias triangles were for example resolved in the QPC conductance signal by Küng [28].

From the measurements of the stability diagrams, we can conclude that our double dots were sufficiently coupled to the leads. It is therefore likely that the reason why we could not observe finite bias triangles was that the tunneling coupling between the dots was too low. In this section, the inter-dot tunneling coupling is investigated in detail on the basis of measurements of samples 07a and 07s.

4.3.1   Plunger gate influence on the tunneling barriers

Generally, the transmission of the tunneling barriers confining the dots is not only influenced by voltages applied to the top gates forming the barriers, but also by other potential changes. In particular, the voltage applied to the plunger gates can have a strong influence on the tunneling barriers. It is, for example, possible that the applied PG voltages in the measurements

Table 2: Settings and current pinch-off voltages obtained in 4.2 K measurements of samples 07s and 07a. Additionally, typical settings of the few electron measurements of sample 06s are provided for comparison.

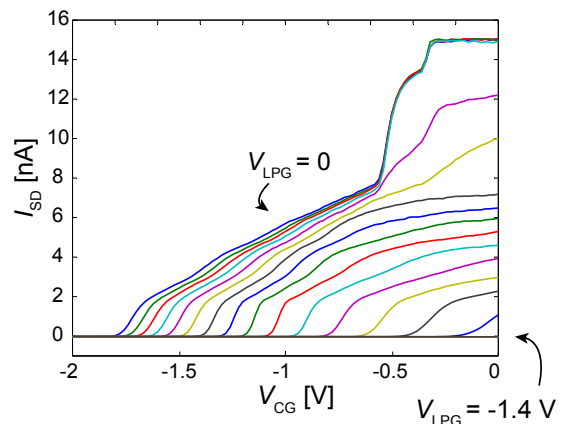| Sample	T	V_{SDB} [V]	V_{CG} [V]	V_{PG} [V]
07s	4.2 K	-0.75	p.o.: -1.80	p.o.: -1.40
07a	4.2 K	-0.75	p.o.: -0.80	p.o.: -0.66
06s	20 mK	-0.77	-0.70	-0.25 to -0.30
+0.3 V pre-bias		≈ -1	≈ -1	

of samples 05 and 06s pinched off the central barrier and prevented inter-dot tunneling. The PG influence on the barriers was investigated in measurements of the samples 07a and 07s at 4.2 K without applied pre-bias.

The center gate and the source drain barrier form a QPC. Current pinch-off curves of this central QPC were measured for different voltages applied to the PGs in order to determine their influence. One data set of sample 07s at 4.2 K is shown in Fig. 33. In the measurements, V_{SDB} was kept at a fixed value of -0.75 V and V_{CG} was swept. This was repeated for different PG voltages between 0 and -2 V. For $V_{\mathrm{PG}} = 0$, the current was pinched off at $V_{\mathrm{CG}} \leq -1.8$ V and for $V_{\mathrm{PG}} \leq -1.4$ V there was no current flow, even for an open CG. This is the value at which the current flow is pinched off between the LPG and the fixed SDB.
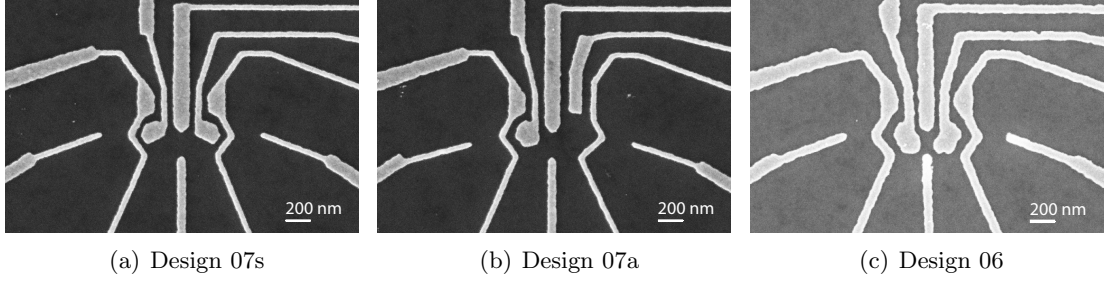
The same measurements were repeated for sample 07a. For this sample, the central QPC was closed for $V_{\mathrm{CG}} \leq -0.80$ V if no PG voltage was applied and the PG pinched off with SDB for $V_{\mathrm{PG}} \leq -0.66$ V. All pinch-off voltages are summarized in table 2. The lower pinch-off voltages for sample 07a can be explained from the different geometry, which is again shown for comparison in Fig. 34. For the asymmetric sample 07a the PG extends farther to the central QPC and comes closer to the SDB.

The analysis of the data collected in these measurements leads to the conclusion that the PG has a stronger influence for the asymmetric sample design due to its larger PG area. In addition, the PG influence on the

Figure 33: Current pinch-off curves of the central QPC of sample 07s for $V_{\mathrm{SDB}} = -0.75$ V and different V_{LPG} measured at 4.2 K.

barriers connecting the dots to the leads was investigated. It is much weaker than the influence on the central barrier, which is again due to the plunger gate shape and position.

A comparison of the sample geometries in Fig. 34 suggests that the PG influence on the central barrier was considerably higher for sample 06s than for both samples 07. The PG influence could not be directly tested for this sample because it was damaged by electrostatic discharge between two cool-downs. However, from the data collected for the samples 07, some conclusions can be drawn about the tunneling coupling in the double dot measurements with sample 06s.

(a) Design 07s   (b) Design 07a   (c) Design 06

Figure 34: Three of the tested designs. The PGs have the smallest area for design 07s and the largest for design 06.

The settings that were used to record the stability diagrams presented in Fig. 30 are given in table 2. For several reasons, these settings cannot be directly compared to those of samples 07s and 07a. First, a pre-bias of $+0.3\,$V was applied to all gates of sample 06s except the PGs. Taking this into account yields voltage settings of SDB and CG, which are roughly equivalent to $1\,$V without pre-bias. Further, the double dots were measured at $20\,$mK and with a charge detector, which means that the sensitivity to current was much higher than in the $4.2\,$K measurements. At $4.2\,$K not even Coulomb peaks can be resolved because $k_{\mathrm{B}}T = 0.4\,$meV ($97\,$GHz) is on the same order of magnitude as the expected charging energy in the samples, therefore the condition for Coulomb blockade is not fulfilled as explained in section 3.

In spite of the difficulties in comparing the data of the different samples, the settings applied in the measurements of sample 06s suggest that the central barrier was closed. This was further enhanced by the fact that two PGs were in operation in the double dot measurements, while it was only one for the $4.2\,$K measurements. The strong influence of the PG geometry on the central barrier that was demonstrated in this section provides strong evidence for a closed central barrier of sample 06s. In conclusion, the presented data supports the speculation that the dots were not sufficiently tunneling coupled in the measurements presented in section 4.2.

The tunneling properties of a single dot were investigated in more detail for the symmetric design 07s at 20 mK. The left dot was coupled to the source by the QPC formed by the SDB and LSG, the source barrier (SB), and to the drain by the central barrier (CB). The tunneling barriers of the left dot (SB and CB) were tuned to be roughly symmetric, when no voltage was applied to the plunger gate. The dot barriers were tuned in the same way for the previously presented double dot measurements. The procedure that was used for tuning the gates for the double dot measurements of samples 05 and 06s is described at length in appendix B.

Coulomb diamonds were recorded with the transconductance signal of the left charge detector. The measured diamonds, which are shown in Fig. 35(a), clearly exhibit an asymmetry. One of the diagonal lines bordering the Coulomb diamonds is much more pronounced than the other. As explained in section 3, each of these lines corresponds to a certain energy level configuration of the quantum dot and the leads. For the case of the strongly pronounced line in Fig. 35(a) a dot level is aligned with the chemical potential of the drain. The reason for the asymmetry in the Coulomb diamonds is an asymmetry in the transmission of the source barrier and central barrier that couple the dot to the leads. In this measurement, the central barrier was much thicker. The corresponding transport situation is schematically shown in Fig. 35(a). Even though the barriers were initially configured roughly symmetrically, the application of negative PG voltages introduced a barrier asymmetry.

(a) $V_{\mathrm{CG}} = -570\,\mathrm{mV}$ (b) $V_{\mathrm{CG}} = -555\,\mathrm{mV}$
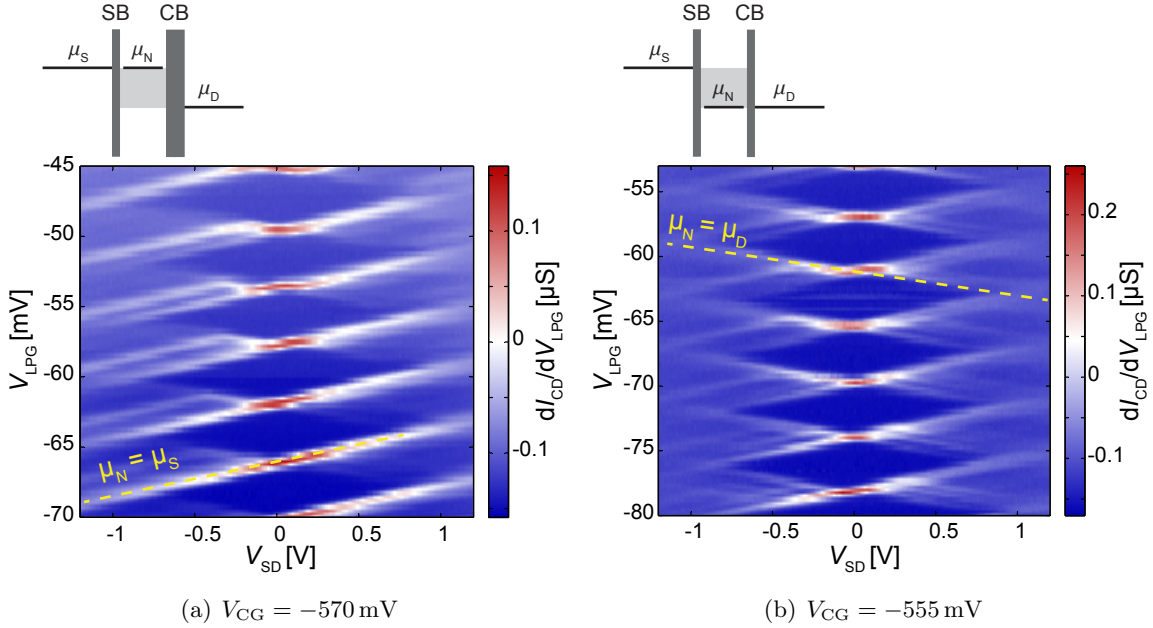
Figure 35: Coulomb diamond measurements of sample 07s in the many electron regime. A clear asymmetry in the visibility of the diagonal lines bordering the diamonds can be observed in (a). For (b) the visibility is much more symmetric. The energy level and barrier configurations of each measurement are depicted on the top.

In order to achieve more symmetric barriers, the measurement was repeated for a less negative CG voltage. The data together with the corresponding transport situation is shown in Fig. 35(b). The visibility of the two lines bordering the diamond is clearly more symmetric than in the first data.

This measurement confirms the conclusion that the plunger gate strongly influences the barrier thickness and has a stronger influence on the central barrier than on the source barrier. Furthermore, the PG voltages applied in these measurements are less negative than those applied in the double dot measurement of sample 06s by roughly 200 mV, for example. From this and the sample geometry, we expect that the central barrier was much thicker than the barriers to the leads in the few electron measurements of sample 06s.

4.3.2 Inter-dot tunneling in few electron measurements

In order to observe finite bias triangles, sufficient inter-dot tunneling coupling is required. Similarly, the observation of Coulomb diamonds requires tunneling coupling to both leads. We could exploit this fact to investigate tunneling through the central barrier with the sample 07s tuned to a single dot configuration. The central barrier of the double dot structure forms the barrier to one of the leads in the single dot. All earlier samples were damaged before the inter-dot tunneling could be studied thoroughly, which is why we had to resort to sample 07s.

The interesting regime for our measurements is the few electron regime. Fig. 36 again shows the few electron Coulomb diamonds that were measured for sample 07s. Careful fine tuning was necessary to achieve these measurements. The CG had to be carefully opened as
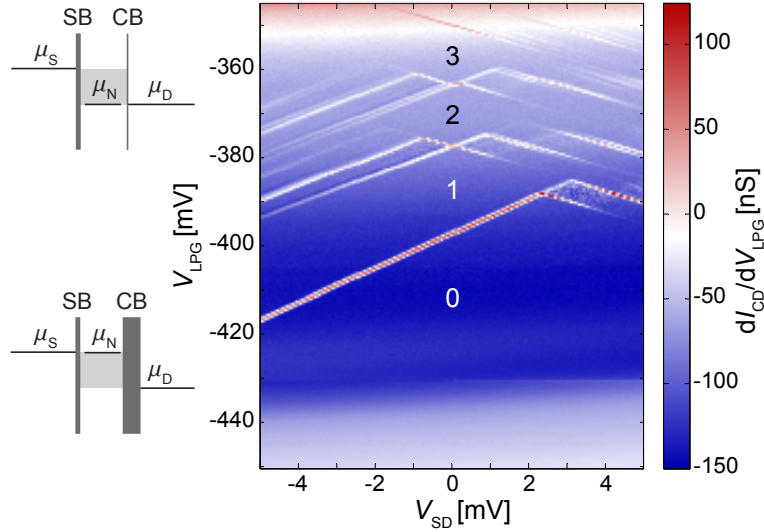
Figure 36: Coulomb diamond measurement of sample 07 in the few electron regime. The transport situations corresponding to the visible lines bordering the diamonds are shown on the left.

more negative PG voltages were applied to empty the dots. As explained in the previous section, this was necessary to keep the thickness of the tunneling barriers symmetric. When V_{CG} was adjusted for more negative LPG voltages, an additional problem became apparent, however: in the presented data the barriers are only opened symmetrically around the diamond corresponding to two electrons in the dot. The last visible line at the bottom corresponds to the transport situation shown at the bottom of Fig. 36. As before, the central barrier has a much higher transmission than the source barrier. Only when a dot state is aligned with the source, electrons can tunnel back and forth through the source barrier and a change in occupation is registered by the detector. The tunneling rate of electrons through the central barrier is too low for the detector to measure a change in occupation.

For $V_{\text{LPG}} \geq -360\,\text{mV}$ the reversed situation is observed. Again, only one of the lines is visible but it is oriented in the other direction. The corresponding energy level scheme is shown at the top in the figure. Now the tunneling rate through the central barrier is too low with respect to that through the source barrier, because the source barrier is less strongly influenced by the PG. In this situation, electrons must be able to tunnel through both barriers but the change in occupation can only be registered for electrons tunneling back and forth through the central barrier that has the higher transmission. Electrons in a dot level aligned with the source leave the dot too quickly through the central barrier to be detected.

In the few electron regime, there is only a narrow range of PG voltages ($\approx 30\,\text{mV}$) in which the dot symmetrically couples to both leads. This region of symmetric tunneling barriers can be shifted up and down in PG voltages by opening VC. It was, for example, also possible to recover both lines at the border between the 0 and 1 electron diamonds. This data is presented in Fig. 38(a) in appendix C. An option to increase this range is to compensate more negative PG voltages with more positive CG voltage in order to keep the central barrier constant. This was attempted, but unfortunately the resulting data did not show any improvements. The compensation measurement is also included in appendix C.

From these measurements we can conclude that a very accurate tuning of the different

barriers is necessary for measurements in the few electron regime. Measurements of complete finite bias triangles require roughly symmetric tunneling barriers between the dots and to both leads. This configuration is difficult to achieve with the samples with extended PGs, especially over a wide range of PG voltages. This is most likely the reason why no finite bias triangles could be observed in the presented double dot measurements.
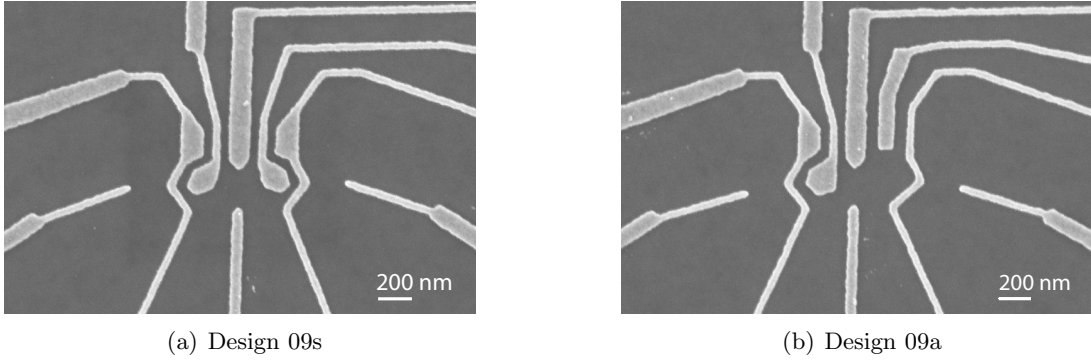
5 Conclusion

The wafer characterization that was presented in part of this thesis yielded useful results that allowed to find new suitable wafers for our quantum dot samples. First wafers from a defective MBE machine were found to have insufficient charge carrier densities and mobilities. After switching supplier, the wafers were suitable in terms of density and mobility. At the same time, a parallel conducting layer was identified in the samples. The influence of the parallel conducting channel was subsequently investigated. The results suggest that the parallel channel should not cause a problem in our measurements, first, because its influence is weak and second because it is further reduced at the low measurement temperatures of our experiments.

In the second and main part of the thesis, new QD sample designs were characterized in few electron measurements. Three of the new designs were tested at low temperature and the characteristic quantities of the double dot system could be extracted. The main difference between the three tested designs was the size and position of the PGs, one of which is intended as the resonator gate in the microwave samples. It was found that the PG design has a very strong influence on the sample properties.

The most relevant sample characteristics are the lever arms of the PGs and the capacitive and tunneling coupling between the dots. The results obtained for the new designs were compared to sample 00 as a reference. This sample had a large lever arm $\alpha_{\mathrm{PG}} = 0.6$, which was in part due to the shallow 2DEG of 35 nm depth instead of 90 nm in the new samples. Its capacitive inter-dot coupling can be quantified by $E_{\mathrm{C,m}} = 0.2 \, \mathrm{meV}$ and $C_{\mathrm{m}} = 4 \, \mathrm{aF}$. Design 05 with the smallest PGs had very low lever arms $\alpha_{\mathrm{PG}} \approx 0.02$. Its capacitive inter-dot coupling was similar to what was found for sample 00. No conclusion can be drawn about the tunneling coupling in this sample because it was damaged before it could be fully tested. Design 06s had extended plunger gates and correspondingly a strongly increased lever arm of $\alpha_{\mathrm{PG}} \approx 0.2$. The capacitive coupling between the dots was reduced by a factor of two with respect to sample 05. From the fact that it was impossible to resolve finite bias triangles, among other indications, it can be suspected that the inter-dot tunneling coupling too low for our purposes. The plunger gates of design 07s had an intermediate extension. Consequently, the lever arm of 0.17 was also reduced with respect to sample 06s, but still on the same order of magnitude. For comparison, all the quantities resulting from the sample characterization are listed again in a table in appendix A.

The influence of the PGs on the inter-dot tunneling coupling was investigated using sample 07s. From the analysis of these results, it can be concluded that extended plunger gates have strong advantages but also disadvantages for forming few electron double dots. On the one hand, a large area of the plunger gates directly entails a large lever arm. This is ultimately desirable to achieve a high coupling strength between the resonator and the QD. In addition, large PGs are convenient for emptying the dots. On the other hand, the plunger gates strongly influence the QPCs coupling the two dots to each and to the leads. In our geometries, the central QPC between the dots was most strongly influenced. Negatively biasing the plunger gates, therefore, significantly reduced inter-dot tunneling coupling. The extended plunger gates proved very useful but need to be designed and operated with caution. Both the high coupling strength g and a sufficient inter-dot tunneling coupling are crucial quantities for our microwave measurements but they are competing goals with respect to the PG geometry. A compromise that makes both possible must be found.

The data presented in this thesis give interesting insights about how such an optimized

(a) Design 09s

(b) Design 09a

Figure 37: Optimized sample geometries of the symmetric and asymmetric designs.

sample should be designed. The drawn conclusions were incorporated in the sample designs 09s and 09a, which are again presented in Fig. 37. The most significant changes with respect to the previous designs are first, that the PGs are smaller and positioned farther away from the central barrier. Second, the designed width of central barrier gap is increased by 35 nm. This design was chosen for the next generation of resonator chips as it is hoped to be suitable for resonator-qubit coupling with few electron quantum dots.

In summary, the double dot designs presented in this thesis could easily be operated in the few electron regime. Additionally, high lever arms were realized by increasing the PG area. It is expected that the final improvements of the sample design that were included in design 09 together with a careful tuning of the tunneling barriers also resolve the encountered problems regarding inter-dot tunneling coupling. Therefore, the goal of this thesis to develop an optimized double quantum dot design for the few electron regime was reached.

A Sample properties

Table 3: Summary of all sample properties that were extracted from the data presented in section 4.2. The values found for samples 05 and 06s were approximated using the single dot lever arms. The listed charging energies cannot be directly compared as they were obtained from measurements with very different numbers of electrons on the dots.

Sample	00	05	06s	07s
α_{LPG} (SQD)		0.022	0.24	0.17
α_{RPG} (SQD)		0.020		
α_{RG} (DQD)	0.6			
$E_{\mathrm{C,L}}$ (SQD)		2.35 meV	0.7 meV	2.3 meV
$E_{\mathrm{C,R}}$ (SQD)		2.33 meV		
$E_{\mathrm{C,L}}$ (DQD)	1.0 meV	4.0 meV	2.9 meV	
$E_{\mathrm{C,R}}$ (DQD)	0.7 meV	3.3 meV	3.1 meV	
$E_{\mathrm{C,m}}$	0.2 meV	0.23 meV	0.1 meV	
$g/2\pi$	50 MHz	≤ 2 MHz	≤ 20 MHz	≤ 15 MHz
C_{m}	4 aF	2.8 aF	1.6 aF	
C_{LPG}	10 aF	0.9 aF	13.3 aF	
C_{RPG}	10 aF	1.0 aF	12.3 aF	
C_{RG}	60 aF			
C_1	34 aF	40 aF	55.6 aF	
C_2	94 aF	44 aF	51.3 aF	

B Formation of double quantum dots

This appendix describes the particular way in which the gates were tuned to form the double quantum dots with samples 05 and 06s. The gate configuration reached in the described way was the basis of all measurements presented in section 4.2.

Determination of critical gate parameters

1. Check of the functionality of all gates.

2. Isolation of the dot from the detector

   To close the gap between the side gates and the drain barriers, the left and right drain barriers (LDB/RDB) are set to strongly negative values (≈ -2 V), then the side gates are swept from 0 V to negative voltages to find current pinch-off values. This provides the voltages $V_{\mathrm{LSG/RSG}}$ which have to be applied to the side gates in subsequent measurements to ensure that no current can flow between the dot and the QPC.

3. Extraction of $V_{\mathrm{LQPC/RQPC}}$ from charge detector pinch-off curve

   Using the optimal $V_{\mathrm{LSG/RSG}}$ found before, a pinch-off curve between the QPC gate and the side gate is recorded. The QPC gate voltage is then chosen in a way that the derivative of the current through the QPC with respect to the QPC top gate,

dI_{CD}/dV_{QPC}, is high to provide good sensitivity. Note that at equivalent slope, the smaller current range will be chosen to limit detector back-action on the dot.

The above derived voltages for LDB/RDB, LSG/RSG and LQPC/RQPC are used as default values in the following steps.

Single dot formation

4. Symmetrical pinch-off of both leads

   The goal is to achieve a symmetric pinch-off of both leads that separate the single dot from source and drain. In our case these barriers are formed between SDB and the center gate (central barrier) and between SDB and one of the side gates (source or drain barrier). Because the side gate voltages are already optimized, the corresponding center gate voltage can be identified from the appropriate pinch-off curves. If the voltages V_{CG} and $V_{LSG/RSG}$ are applied, SDB symmetrically closes both leads, to a good approximation. We can thus form a single dot separated from the leads by roughly symmetric tunnel barriers.

5. 2D map of the Coulomb peaks depending on the PG and SDB voltage

   One now investigates the SDB/PG dependence of the current through the single dot. Ideally, Coulomb peaks emerge as a function of the PG voltage for certain values of SDB. A single quantum dot is then formed at a suitable SDB voltage and can be characterized in Coulomb diamond measurements.

6. Coulomb diamonds

   At the working point found in step 5, a 2D map of the derivative of the current through the dot with respect to the applied bias, dI_{SD}/dV_{SD} can be recorded while sweeping V_{SD} and stepping the plunger gate voltage.

Double dot formation

7. Current measurement with the charge detector

   As in the case of the single dot (see 4.), one would like to couple symmetrically to both leads. For the double dot the relevant barriers are formed between SDB and LSG, respectively RSG. The voltages that have to be applied to LSG and RSG to achieve the symmetric pinch-off usually differ slightly. These settings are used together with the voltage parameters determined earlier. In this configuration, the side gates, CG and SDB form a double dot, which can be characterized using either the left or right QPC as charge detector. The charge detector current I_{CD} is recorded while sweeping V_{LPG} for different V_{RPG} values or vice-versa, which yields a 2D current stability diagram.

8. Stability diagrams from transconductance measurements

   In regions of the current stability diagram in which the detector current is too small to resolve the honeycomb pattern, a transconductance measurement of the double dot can be used for higher sensitivity. An AC modulation is applied to one of the plunger gates and dI_{CD}/dV_{PG} is plotted in a 2D map while both plunger gates are swept. We chose to modulate the LPG while measuring with the right charge detector or vice versa but other

configurations are also possible. For our samples, only transconductance measurements allow to resolve the few electron regime in the stability diagram.

C   Compensation

In few electron Coulomb diamond measurements of sample 07s, a problem became apparent. The tunneling barriers to the two leads of the single dot only had a symmetric thickness for a small range of PG voltages. The reasons for this behavior were explained in section 4.3.2. In order to increase the PG range of symmetric coupling to the leads, compensation measurements were tried in which the CG was opened at the same rate at which the influence of LPG closed the central barrier. From current pinch-off curves, the rate at which the CG needs to be opened was determined as: $V_{CG} = -0.55\,V_{LPG} - 0.60\,\text{V}$.

In Fig. 38(a) a measurement without compensation for a fixed $V_{CG} = -365\,\text{mV}$ is shown. For this setting, the lines in both directions corresponding to symmetric coupling to the leads were only visible between the 0 and 1 electron diamonds. The measurement was repeated with the same settings but with the compensation formula applied for V_{CG}. It can be seen that the compensation did not notably increase the PG voltage range for which the barriers are symmetric. The only effect was that the diamonds were slightly stretched in V_{LPG}-direction. This is illustrated by the voltage dimensions indicated in the figures.

(a) $V_{CG} = -365\,\text{mV}$ (b) Compensation
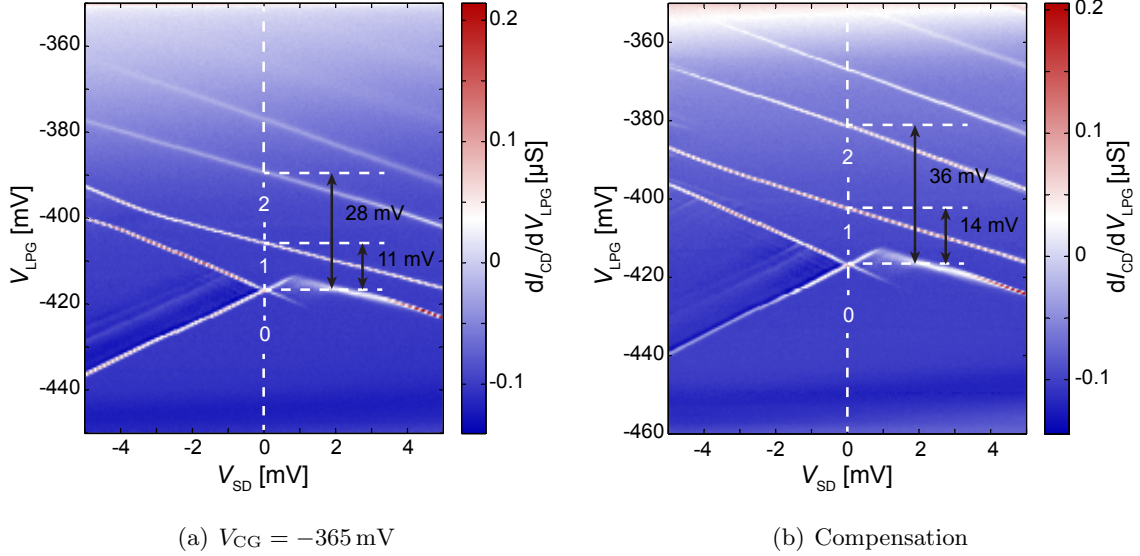
Figure 38: Coulomb diamond measurements of sample 07s in the few electron regime. Measurement (a) was recorded for a fixed CG voltage, while the CG voltage was varied with V_{LPG} in measurement (b) according to $V_{CG} = -0.55\,V_{LPG} - 0.60\,\text{V}$.

References

[1] T. Frey, P. J. Leek, M. Beck, A. Blais, T. Ihn, K. Ensslin, and A. Wallraff. Dipole coupling of a double quantum dot to a microwave resonator. *Phys. Rev. Lett.*, 108:046807, 2012.

[2] D. I. Schuster. *Circuit Quantum Electrodynamics*. PhD thesis, Yale University, 2007.

[3] S. Haroche and J.-M. Raimond. *Exploring the Quantum: Atoms, Cavities, and Photons.* Oxford University Press, 2006.

[4] H. Mabuchi and A. C. Doherty. Cavity quantum electrodynamics: Coherence in context. *Science*, 298:1372–1377, 2002.

[5] M. A. Nielsen and I. L. Chuang. *Quantum Computation and Quantum Information.* Cambridge University Press, 2000.

[6] A. Wallraff, D. I. Schuster, A. Blais, L. Frunzio, R.-S. Huang, J. Majer, S. Kumar, S. M. Girvin, and R. J. Schoelkopf. Strong coupling of a single photon to a superconducting qubit using circuit quantum electrodynamics. *Nature*, 431:162–167, 2004.

[7] A. Fedorov, L. Steffen, M. Baur, M. P. da Silva, and A. Wallraff. Implementation of a toffoli gate with superconducting circuits. *Nature*, 481:170–172, 2012.

[8] M. Baur, A. Fedorov, L. Steffen, S. Filipp, M. P. da Silva, and A. Wallraff. Benchmarking a quantum teleportation protocol in superconducting circuits using tomography and an entanglement witness. *Phys. Rev. Lett.*, 108:040502, 2012.

[9] L. Childress, A. S. Sørensen, and M. D. Lukin. Mesoscopic cavity quantum electrodynamics with quantum dots. *Phys. Rev. A*, 69:042302, 2004.

[10] T. Frey, P. J. Leek, M. Beck, K. Ensslin, A. Wallraff, and T. Ihn. Characterization of a microwave frequency resonator via a nearby quantum dot. *Appl. Phys. Lett.*, 98:262105, 2011.

[11] A. Blais, R.-S. Huang, A. Wallraff, S. M. Girvin, and R. J. Schoelkopf. Cavity quantum electrodynamics for superconducting electrical circuits: An architecture for quantum computation. *Phys. Rev. A*, 69:062320, 2004.

[12] L. P. Kouwenhoven, C. M. Marcus, P. L. McEuen, S. Tarucha, R. M. Westervelt, and N. S. Wingreenj. Electron transport in quantum dots. *Proceedings of the NATO Advanced Study Institute on Mesoscopic Electron Transport, edited by L. L. Sohn, L. P. Kouwenhoven, and G. Schön, Kluwer Series*, E345:105–214, 1997.

[13] M. Göppl, A. Fragner, M. Baur, R. Bianchetti, S. Filipp, J. M. Fink, P. J. Leek, G. Puebla, L. Steffen, and A. Wallraff. Coplanar waveguide resonators for circuit quantum electrodynamics. *J. Appl. Phys.*, 104:113904, 2008.

[14] D. M. Pozar. *Microwave engineering.* Wiley, second edition, 1998.

[15] T. Frey, P. J. Leek, M. Beck, J. Faist, A. Wallraff, K. Ensslin, T. Ihn, and M. Büttiker. Quantum dot admittance probed at microwave frequencies with an on-chip resonator. *arXiv:1207.0945v1*, 2012.

[16] W. G. van der Wiel, S. De Franceschi, J. M. Elzerman, T. Fujisawa, S. Tarucha, and L. P. Kouwenhoven. Electron transport through double quantum dots. *Rev. Mod. Phys.*, 75:1–22, 2002.

[17] B. A. Joyce. Molecular beam epitaxy. *Rep. Prog. Phys.*, 48:1637 – 1697, 1985.

[18] M. B. Panish. Molecular beam epitaxy. *Science*, 208:916–922, 1980.

[19] T. Ihn. *Semiconductor nanostructures*. Oxford University Press, 2010.

[20] Y. V. Nazarov and Y. M. Blanter. *Quantum Transport: Introduction to Nanoscience*. Cambridge University Press, 2009.

[21] K. v. Klitzing, G. Dorda, and M. Pepper. New method for high-accuracy determination of the fine-structure constant based on quantized hall resistance. *Phys. Rev. Lett.*, 45:494–497, 1980.

[22] G. Salis. *Electronic Properties of Tailored Semiconductor Nanostructes with Tunable Dimensionality*. Diss. ETH No. 12976, ETH Zurich, 1999.

[23] H. van Houten, J. G. Williamson, M. E. I. Broekaart, C. T. Foxon, and J. J. Harris. Magnetoresistance in GaAs-Al$_x$Ga$_{1-x}$As heterostructure with double subband occupancy. *Phys. Rev. B.*, 37:2756 – 2758, 1988.

[24] D. V. Averin and A. A. Odintsov. Macroscopic quantum tunneling of the electric charge in small tunnel junctions. *Phys. Lett. A*, 140:251 – 257, 1989.

[25] D. V. Averin and Y. V. Nazarov. Virtual electron diffusion during quantum tunneling of the electric charge. *Phys. Rev. Lett.*, 65:2446–2449, 1990.

[26] M. Field, C. G. Smith, M. Pepper, D. A. Ritchie, J. E. F. Frost, G. A. C. Jones, and D. G. Hasko. Measurements of Coulomb blockade with a noninvasive voltage probe. *Phys. Rev. Lett.*, 70:1311–1314, 1993.

[27] M. Pioro-Ladrière, J. H. Davies, A. R. Long, A. S. Sachrajda, L. Gaudreau, P. Zawadzki, J. Lapointe, J. Gupta, Z. Wasilewski, and S. Studenikin. Origin of switching noise in GaAs/Al$_x$Ga$_{1-x}$As lateral gated devices. *Phys. Rev. B*, 72:115331, 2005.

[28] B. Küng. *Statistics of charge fluctuations in semiconductor nanostructures*. Diss. ETH No. 20234, ETH Zurich, 2012.